

ViTAL: Vision-Based Terrain-Aware Locomotion for Legged Robots

Shamel Fahmi, Victor Barasuol, Domingo Esteban, Octavio Villarreal, and Claudio Semini

Abstract—This work is on vision-based planning strategies for legged robots that separate locomotion planning into foothold selection and pose adaptation. Current pose adaptation strategies optimize the robot’s body pose relative to *given* footholds. If these footholds are not reached, the robot may end up in a state with no reachable safe footholds. Therefore, we present a **Vision-Based Terrain-Aware Locomotion (ViTAL)** strategy that consists of novel pose adaptation and foothold selection algorithms. **ViTAL** introduces a different paradigm in pose adaptation that does not optimize the body pose relative to given footholds, but the body pose that maximizes the chances of the legs in reaching safe footholds. **ViTAL** plans footholds and poses based on skills that characterize the robot’s capabilities and its terrain-awareness. We use the 90 kg **HyQ** and 140 kg **HyQReal** quadruped robots to validate **ViTAL**, and show that they are able to climb various obstacles including stairs, gaps, and rough terrains at different speeds and gaits. We compare **ViTAL** with a baseline strategy that selects the robot pose based on given selected footholds, and show that **ViTAL** outperforms the baseline.

Index Terms—Legged Robots, Whole-Body Motion Planning and Control, Visual Learning, Optimization and Optimal Control

I. INTRODUCTION

LEGGED robots have shown remarkable agile capabilities in academia [1]–[6] and industry [7]–[9]. Yet, to accomplish breakthroughs in dynamic whole-body locomotion, and to robustly traverse unexplored environments, legged robots have to be *terrain aware*. **Terrain-Aware Locomotion (TAL)** implies that the robot is capable of taking decisions based on the terrain [10]. The decisions can be in planning, control, or in state estimation, and the terrain may vary in its geometry and physical properties [11]–[19]. **TAL** allows the robot to use its on-board sensors to perceive its surroundings and act accordingly. This work is on *vision-based TAL planning strategies* that plan the robot’s motion (body and feet) based on the terrain information that is acquired using vision (see Fig. 1).

A. Related Work - Vision-Based Locomotion Planning

Vision-based locomotion planning can either be *coupled* or *decoupled*. The coupled approach jointly plans the body pose and footholds in a single algorithm. The decoupled approach independently plans the body pose and footholds in separate algorithms. The challenge in the coupled approach

Manuscript received November 23, 2021; accepted November 7, 2022. This article was recommended for publication by Associate Editor J. Kober and Editor E. Yoshida upon evaluation of the reviewers’ comments. (*Corresponding author: Shamel Fahmi*)

The authors are with the Dynamic Legged Systems Lab, Istituto Italiano di Tecnologia (IIT), Genova, Italy (email: firstname.lastname@iit.it).

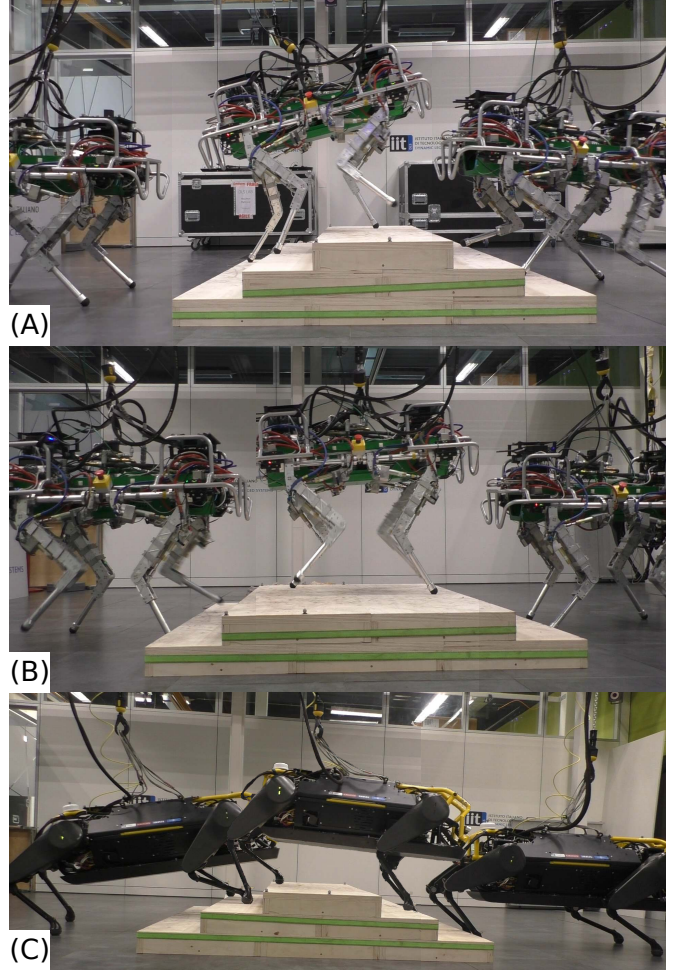


Fig. 1. The **HyQ** and **HyQReal** quadruped robots climbing stairs using **ViTAL**.

is that it is computationally expensive to solve in real-time. Because of this, the decoupled approach tends to be more practical since the high-dimensional planning problem is split into multiple low-dimensional problems. This also makes the locomotion planning problem more tractable. However, this raises an issue with the decoupled approach because the plans may conflict with each other since they are planned separately. Note that both approaches could be solved using optimization, learning, or heuristic methods.

Trajectory Optimization (TO) is one way to deal with coupled vision-based locomotion planning. By casting locomotion planning as an optimal control problem, **TO** methods can optimize the robot’s motion while taking into account the terrain information [20]–[24]. The locomotion planner can generate

trajectories that prevent the robot from slipping or colliding with the terrain by encoding the terrain's shape and friction properties in the optimization problem [24]. **TO** methods can also include a model of the terrain as a cost map in the optimization problem, and generate the robot's trajectories based on that [25]. **TO** methods provide guarantees on the optimality and feasibility of the devised motions, albeit being computationally expensive; performing these optimizations in real-time is still a challenge. To overcome this issue, **TO** approaches often implement hierarchical (decoupled) approaches. Instead of decoupling the plan into body pose and footholds, the hierarchical approaches decouple the plan into short and long-horizon plans [26], [27]. Additionally, other work relies on varying the model complexity to overcome the computational issue with **TO** [28].

Reinforcement Learning (RL) methods mitigate the computational burden of **TO** methods by training function approximators that learn the locomotion plan [29]–[35]. Once trained, an **RL** policy can generate body pose and foothold sequences based on proprioceptive and/or visual information. Yet, **RL** methods may require tedious learning (large amounts of data and training time) given its high-dimensional state representations.

As explained earlier, decoupled locomotion planning can mitigate the problems of **TO** and **RL** by separating the locomotion plan into feet planning and body planning [36]–[41]. Thus, one can develop a more refined and tractable algorithm for every module separately. In this work, planning the feet motion (foothold locations) is called *foothold selection*, and planning the body motion is called *pose adaptation*.

B. Related Work - Foothold Selection and Pose Adaptation

Foothold selection strategies choose the best footholds based on the terrain information and the robot's capabilities. Early work on foothold selection was presented by Kolter *et al.* [42] and Kalakrishnan *et al.* [43] where both approaches relied on motion capture systems and an expert user to select (label) the footholds. These works were then extended in [44] using unsupervised learning, on-board sensors, and considered the terrain information such as the terrain roughness (to avoid edges and corners) and friction (to avoid slippage). Then, Barasuol *et al.* [45] extended the aforementioned work by selecting footholds that not only considers the terrain morphology, but also considering leg collisions with the terrain. Further improvements in foothold selection strategies added other evaluation criteria such as the robot's kinematic limits. These strategies use optimization [37], [46], [47], supervised learning [38], [48], [49], **RL** [1], [17], or heuristic [50] methods.

Similar to foothold selection, pose adaptation strategies optimize the robot's body pose based on the terrain information and the robot's capabilities. An early work on vision-based pose adaptation was presented in [36]. The goal was to find the optimal pose that maximizes the reachability of *given* selected footholds, avoid collisions with the terrain, and maintain static stability. The given footholds are based on a foothold selection algorithm that considers the terrain geometry. Another

approach was presented in [51] that finds the optimal body elevation and inclination *given* the selected footholds, and the robot location in the map. The pose optimizer maximizes different margins that increase the kinematic reachability of the legs and static stability, and avoids terrain collisions. This approach was then extended in [52] with an improved version of the kinematic margins. A similar approach was presented in [37] where the goal was to find an optimal pose that can maximize the reachability of *given* selected footholds. The reachability term is accounted for in the cost function of the optimizer by penalizing the difference between the default foothold position and the selected one. The work in [39] builds on top of the pose optimizer of [37] to adapt the pose of the robot in confined spaces using 3D terrain maps. This is done using a hierarchical approach that first samples body poses that allows the robot to navigate through confined spaces, then smooths these poses using a gradient descent method that is then augmented with the pose optimizer of [37]. The work presented in [53] generates vision-based pose references that also rely on *given* selected footholds to estimate the orientation of the terrain and send it as a pose reference. Alongside the orientation reference, the body height reference is set at a constant vertical distance (parallel to gravity) from the center of the approximated plane that fits through the selected footholds.

The aforementioned pose adaptation strategies focus on finding *one* optimal solution based on *given* footholds; footholds have to be first selected and *given* to the optimizer. Despite selecting footholds that are safe, there are no guarantees on what would happen during execution if the footholds are not reached or if the robot deviates from its planned motion. If any of these cases happen, the robot might end up in a pose where no safe footholds can be reached. This would in turn compromise the safety and performance of the robot. Even if the strategy can re-plan, reaching a safe pose might not be possible if the robot is already in an unsafe state.

C. Proposed Approach

We propose **Vision-Based Terrain-Aware Locomotion (ViTAL)**, an online whole-body locomotion planning strategy that consists of a foothold selection and a pose adaptation algorithm. The foothold selection algorithm used in this work is an extension of the **Vision-Based Foothold Adaptation (VFA)** algorithm of the previous work done by Villarreal *et al.* [38] and Esteban *et al.* [49]. Most importantly, we propose a novel **Vision-Based Pose Adaptation (VPA)** algorithm that introduces a different paradigm to overcome the drawbacks of the state-of-the-art pose adaptation methods. *Instead of finding body poses that are optimal for given footholds, we propose finding body poses that maximize the chances of reaching safe footholds in the first place.* Hence, we are interested in putting the robot in a state in which if it deviates from its planned motion, the robot remains around a set of footholds that are still reachable and safe. The notion of safety emerges from skills that characterize the robot's capabilities.

ViTAL plans footholds and body poses by sharing the same robot skills (both for the **VPA** and the **VFA**). These skills

characterize what the robot is capable of doing. The skills include, but are not limited to: the robot's ability to avoid edges, corners, or gaps (*terrain roughness*), the robot's ability to remain within the workspace of the legs during the swing and stance phases (*kinematic limits*), and the robot's ability to avoid colliding with the terrain (*leg collision*). These skills are denoted by *Foothold Evaluation Criteria (FEC)*. Evaluating the *FEC* is usually computationally expensive. Thus, to incorporate the *FEC* in *VITAL*, we rely on approximating them with *Convolutional Neural Networks (CNNs)* that are trained via supervised learning. This allows us to continuously adapt both the footholds and the body pose. The *VFA* and the *VPA* are decoupled and can run at a different update rate. However, they are non-hierarchical, they run in parallel, and they share the same knowledge of the robot skills (the *FEC*). By that, we overcome the limitations that result from hierarchical planners as mentioned in [39], where high-level plans may conflict with the low-level ones causing a different robot behavior.

The *VPA* utilizes the *FEC* to approximate a function that provides the number of safe footholds for the legs. Using this function, we cast a *pose optimizer* which solves a nonlinear optimization problem that maximizes the number of safe footholds for all the legs subject to constraints added to the robot pose. The pose optimizer is a key element in the *VPA* since it adds safety layers and constraints to the learning part of our approach. This makes our approach more tractable which mitigates the issues that might arise from end-to-end policies in *RL* methods.

D. Contributions

VITAL mitigates the above-mentioned conflicts that exist in other decoupled planners [37], [39], [41], [46]. This is because both the *VPA* and the *VFA* share the same skills encoded in the *FEC*. In other words, the *VPA* and the *VFA* will not plan body poses and footholds that may conflict with each other because both planners share the same logic. In this work, the formulation of the *VPA* allows *VITAL* to reason about the leg's capabilities and the terrain information. However, the formulation of the *VPA* could be further augmented by other body-specific skills. For instance, the *VPA* could be reformulated to reason about the body collisions with the environment similar to the work in [41], [54]. The paradigm of the *FEC* can also be further augmented to consider other skills. We envision that some skills are best encoded via heuristics while others are well suited through optimization. For this reason, the *FEC* can also handle optimization-based foothold objectives such as the ones in [46].

Following the recent impressive results in *RL*-based locomotion controllers, we envision *VITAL* to be inserted as a module into such control frameworks. To elaborate, current *RL*-based locomotion controllers [1], [29], [31], [33] are of a single network; the *RL* framework is a single policy that maps the observations (proprioceptive and exteroceptive) to the actions. This may be challenging since it requires careful reward shaping, and generalizing to new tasks or different sensors (observations) makes the problem harder [55]. For this reason, and similar to Green *et al.* [55], we envision

that *VITAL* can be utilized as a planner for *RL* controllers where the *RL* controller will act as a reactive controller that then receives guided (planned) commands in a form of optimal poses and footholds from *VITAL*.

VITAL differs from *TO* and optimization-based methods in several aspects. The *FEC* is designed to independently evaluate every skill (criterion). Thus, one criterion can be optimization-based while other could be using logic or heuristics. Because of this, *VITAL* is not restricted by solving an optimization problem that handles all the skills at once. Another difference between *VITAL* and *TO* is in the way the body poses are optimized. In *TO*, the optimization problem optimizes a single pose to follow a certain trajectory. The *VPA* in *VITAL* optimizes for the body poses that maximizes the chances of the legs in reaching safe footholds. In other words, the *VPA* finds a body pose that would put the robot in a configuration where the legs have the maximum possible number of safe footholds. In fact, this paradigm that the *VPA* of *VITAL* introduces may be also encoded in *TO*. Additionally, *TO* often finds body poses that considers the leg's workspace, but to the best of the authors' knowledge, there is no *TO* method that finds body poses that consider the legs' collision with the terrain, and the feasibility of the swinging legs' trajectory.

To that end, the *contributions* of this article are

- *VITAL*, an online vision-based locomotion planning strategy that simultaneously plans body poses and footholds based on shared knowledge of robot skills (the *FEC*).
- An extension of our previous work on the *VFA* algorithm for foothold selection that considers the robot's body twist and the gait parameters.
- A novel pose adaptation algorithm called the *VPA* that finds the body pose that maximizes the number of safe footholds for the robot's legs.

II. FOOTHOLD EVALUATION CRITERIA (FEC)

The *FEC* is main the building block for the *VFA* and the *VPA*. The *FEC* are sets of skills that evaluate footholds within heightmaps. The skills include the robot's ability to assess the terrain's geometry, avoid leg collisions, and avoid reaching kinematic limits. The *FEC* can be model-based as in this work and [36], [38], or using optimization techniques as in [37], [46]. The *FEC* of this work extends the criteria used in our previous work [38], [45], [49].

The *FEC* takes a tuple T as an input, evaluates it based on multiple criteria, and outputs a boolean matrix μ_{safe} . The input tuple T is defined as

$$T = (H, z_h, v_b, \alpha) \quad (1)$$

where $H \in \mathbb{R}^{h_x \times h_y}$ is the heightmap of dimensions h_x and h_y , $z_h \in \mathbb{R}$ is the *hip height* of the leg (in the world frame), $v_b \in \mathbb{R}^6$ is the base twist, and α are the gait parameters (step length, step frequency, duty factor, and time remaining till touchdown). The heightmap H is extracted from the terrain elevation map, and is oriented with respect to the horizontal frame of the robot [56]. The horizontal frame coincides with the base frame of the robot, and its xy -plane is perpendicular to the gravity vector. Each cell (pixel) of H denotes the terrain

height that corresponds to the location of this cell in the terrain map. Each cell of H also corresponds to a *candidate foothold* $p_c \in \mathbb{R}^3$ for the robot.

In this work, we only consider the following **FEC**: *Terrain Roughness (TR)*, *Leg Collision (LC)*, *Kinematic Feasibility (KF)*, and *Foot Trajectory Collision (FC)*. Each criterion C outputs a boolean matrix μ_C . Once all of the criteria are evaluated, the final output μ_{safe} is the element-wise logical AND (\wedge) of all the criteria. The output matrix $\mu_{\text{safe}} \in \mathbb{R}^{h_x \times h_y}$ is a boolean matrix with the same size as the input heightmap H . μ_{safe} indicates the candidate footholds (elements in the heightmap H) that are *safe*. An element in the matrix μ_{safe} that is true, corresponds to a candidate foothold p_c in the heightmap H that is safe. The output of the **FEC** is

$$\mu_{\text{safe}} = \mu_{\text{TR}} \wedge \mu_{\text{LC}} \wedge \mu_{\text{KF}} \wedge \mu_{\text{FC}}. \quad (2)$$

An overview of the criteria used in this work is shown in Fig. 2(A) and is detailed below.

Terrain Roughness (TR). This criterion checks edges or corners in the heightmap that are unsafe for the robot to step on. For each candidate foothold p_c in H , we evaluate the mean and standard deviation of the slope relative to its neighboring footholds, and put a threshold that defines whether a p_c is safe or not. Footholds above this threshold are discarded.

Leg Collision (LC). This criterion selects footholds that do not result in leg collision with the terrain during the entire gait cycle (from lift-off, during swinging, touchdown and till the next lift-off). To do so, we create a bounding region around the leg configuration that corresponds to the candidate foothold p_c and the current hip location. Then, we check if the bounding region collides with the terrain (the heightmap) by measuring the closest distance between them. If this distance is lower than a certain value, then the candidate foothold is discarded.

Kinematic Feasibility (KF). This criterion selects footholds that are kinematically feasible. It checks whether a candidate foothold p_c will result in a trajectory that remains within the workspace of the leg during the entire gait cycle. To do so, we check if the candidate foothold p_c is within the workspace of the leg during touchdown and next lift-off. Also, we check if the trajectory of the foot from the lift-off position p_{lo} till the touchdown position at the candidate foothold p_c is within the workspace of the leg. In the initial implementation in [38], this criterion was only evaluated during touchdown. In this work, we consider this criterion during the entire leg step-cycle.

Foot Trajectory Collision (FC). This criterion selects footholds that do not result in foot trajectory collision with the terrain. It checks whether the foot swing trajectory corresponding to a candidate foothold p_c is going to collide with the terrain or not. If the swing trajectory collides with the terrain, the candidate foothold p_c is discarded.

Remark 1: There are three main sources of uncertainty that can affect the foothold placement [45]. These sources of uncertainty are due to trajectory tracking errors, foothold prediction errors, and drifts in the map. To allow for a degree of uncertainty, after computing μ_{safe} , candidate footholds that are within a radius of unsafe footholds are also discarded. This is similar to the erosion operation in image processing.

Remark 2: The initial implementation of the **FEC** in [38] only considered the heightmap H as an input; the other inputs of the tuple T in (1) were kept constant. This had a few disadvantages that we reported in [49] where we extended the work of [38] by considering the linear body heading velocity. In this work, we build upon that by considering the full body twist v_b and the gait parameters α as expressed by T in (1).

III. VISION-BASED FOOTHOLD ADAPTATION (VFA)

The **VFA** evaluates the **FEC** to select the optimal foothold for each leg [38], [45], [49]. The **VFA** has three main stages as shown in Fig. 2(B): *heightmap extraction*, *foothold evaluation*, and *trajectory adjustment*.

Heightmap Extraction. Using the current robot states and gait parameters, we estimate the touchdown position of the swinging foot in the world frame as detailed in [38]. This is denoted as the *nominal foothold* $p_n \in \mathbb{R}^3$. Then, we extract a heightmap H_{vfa} that is centered around p_n .

Foothold Evaluation. After extracting the heightmap, we compute the *optimal foothold* $p_* \in \mathbb{R}^3$ for each leg. We denote this by foothold evaluation which is the mapping

$$g(T_{\text{vfa}}) : T_{\text{vfa}} \rightarrow p_* \quad (3)$$

that takes an input tuple T_{vfa} that is defined as

$$T_{\text{vfa}} = (H_{\text{vfa}}, z_h, v_b, \alpha, p_n). \quad (4)$$

Once we evaluate the **FEC** in (2), from all of the safe candidate footholds in μ_{safe} , we select the optimal foothold p_* as the one that is *closest to the nominal* foothold p_n . The aim is to minimize the deviation from the original trajectory and thus results in a less disturbed or aggressive motion. An overview of the foothold evaluation stage is shown in Fig. 3 where the tuple T of the **FEC** in (1) is extracted from the **VFA** tuple T_{vfa} in (4) to compute μ_{safe} . Then, using p_n and μ_{safe} , we extract p_* as the safe foothold that is closest to p_n .

Trajectory Adjustment. The leg's swinging trajectory is adjusted once p_* is computed.

Remark 3: To compute the foothold evaluation, one can directly apply the exact mapping $g(T_{\text{vfa}})$. Yet, computing the foothold evaluation leads to evaluating the **FEC** which is generally computationally expensive. Thus, to speed up the computation and to continuously run the **VFA** online, we train a **CNN** to approximate the foothold evaluation $\hat{g}(T_{\text{vfa}})$ using supervised learning. Once trained, the **VFA** can then be executed online using the **CNN**. The **CNN** architecture of the foothold evaluation is explained in Appendix A.

IV. VISION-BASED POSE ADAPTATION (VPA)

The **VPA** generates pose references that maximize the chances of the legs to reach safe footholds. This means that the robot pose has to be aware of what the legs are capable of and adapt accordingly. Therefore, the goal of the **VPA** is to adapt the robot pose based on the same set of skills in the **FEC** used by the **VFA**.

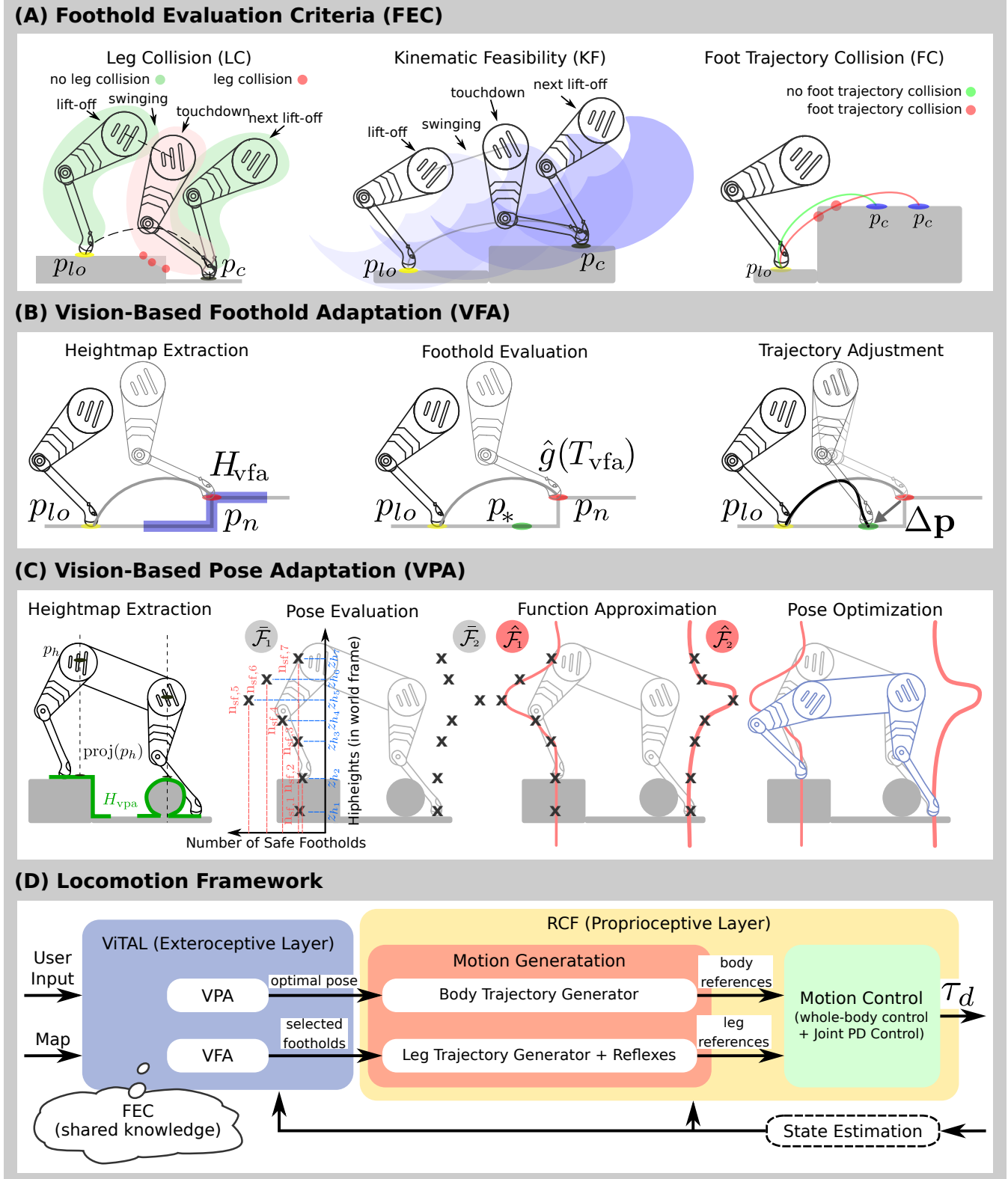


Fig. 2. Overview of **ViTAL**. Illustrations are not to scale. (A) The Foothold Evaluation Criteria (**FEC**): Leg Collision (LC), Kinematic Feasibility (KF), and Foot Trajectory Collision (FC). (B) The Vision-based Foothold Adaptation (VFA) pipeline. First, we extract the heightmap H_{vfa} around the nominal foothold p_n . Then, we evaluate the heightmap either using the exact evaluation $g(T_{vfa})$ or using the CNN as an approximation $\hat{g}(T_{vfa})$. Once the optimal foothold p_* is selected, the swing trajectory is adjusted. (C) The Vision-Based Pose Adaptation (VPA) pipeline. First, we extract the heightmap H_{vpa} for all the legs. The heightmaps are centered around the projection of the leg hip locations. Then, we evaluate the **FEC** to compute $\bar{\mathcal{F}}$ for all the hip heights of all the legs (pose evaluation). Then, we approximate a continuous function $\hat{\mathcal{F}}$ from $\bar{\mathcal{F}}$ (function approximation). The pose optimizer finds the pose that maximizes $\hat{\mathcal{F}}$ for all of the legs (pose optimization). (D) Our locomotion framework. **ViTAL** consists of the **VPA** and the **VFA** algorithms. Both algorithms rely on the robot skills which we denote by **FEC**. τ_d are the desired joint torques that are sent to the robot.

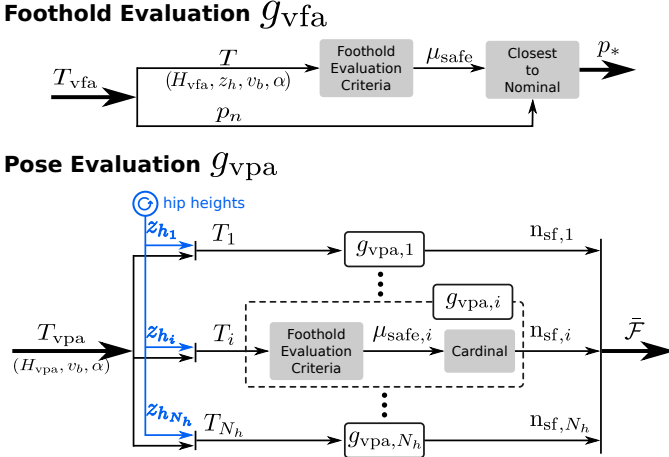


Fig. 3. Overview of the foothold evaluation stage in the VFA algorithm, and the pose evaluation stage in the VPA algorithm.

A. Definitions and Notations

Number of Safe Footholds. As explained earlier, the **FEC** takes a tuple T as an input and outputs the matrix μ_{safe} . Based on that, let us define the **Number of Safe Footholds** (n_{sf})

$$n_{\text{sf}} := \text{cardinal}(\{e \in \mu_{\text{safe}} : e = 1\}) \quad (5)$$

as the number of *true* elements in the boolean matrix μ_{safe} .

Set of Safe Footholds. Consider a set of tuples \mathcal{T} where each element $T_i \in \mathcal{T}$ is a tuple defined as

$$T_i = (H, z_{h_i}, v_b, \alpha) \quad (6)$$

and $z_{h_i} \in \mathcal{Z}$ is a hip height element in the set of hip heights \mathcal{Z} (in the world frame). All the tuple elements $T_i \in \mathcal{T}$ share the same heightmap H , body twist v_b and gait parameters α .

Evaluating the **FEC** in (2) for every $T_i \in \mathcal{T}$ that corresponds to $z_{h_i} \in \mathcal{Z}$, and computing the cardinal in (5) yields $n_{\text{sf},i}$ for every T_i . This yields the **Set of Safe Footholds** (\mathcal{F}) which is a set containing the number of safe footholds n_{sf} that are evaluated based on the **FEC** given the set of tuples \mathcal{T} that corresponds to the set of hip heights \mathcal{Z} but shares the same heightmap H , body twist v_b and gait parameters α .

B. From the Set of Safe Footholds to Pose Evaluation

The set of safe footholds \mathcal{F} is one of the building blocks of the **VPA**. To compute \mathcal{F} , we compute the input tuple T_{vpa}

$$T_{\text{vpa}} = (H_{\text{vpa}}, v_b, \alpha) \quad (7)$$

that we then augment with the hip heights z_{h_i} in the hip heights set \mathcal{Z} yielding the set of tuples \mathcal{T} . Then, we evaluate the **FEC** in (2) for every $T_i \in \mathcal{T}$, and computing the cardinal in (5). This can be expressed by the mapping

$$g_{\text{vpa}}(T_{\text{vpa}}) : T_{\text{vpa}} \rightarrow \mathcal{F} \quad (8)$$

which is referred to as *pose evaluation*. We can express \mathcal{F} as

$$\mathcal{F} = \{n_{\text{sf},i} = g_{\text{vpa},i}(T_i) \forall T_i \in \mathcal{T}\}. \quad (9)$$

Remark 4: Since \mathcal{Z} is an infinite continuous set, so is \mathcal{F} which is not numerically feasible to compute. Hence, we

sample a finite set $\bar{\mathcal{Z}}$ of N_{z_h} samples of hip heights that results in a finite set of safe footholds $\bar{\mathcal{F}}$. To use the set of safe footholds in an optimization problem, we need a continuous function. Thus, after we compute $\bar{\mathcal{F}}$, we estimate a continuous function $\hat{\mathcal{F}}$ as explained next.

An overview of the pose evaluation is shown in Fig. 3 where the tuple T_{vpa} in (7) is augmented with the hip heights z_{h_i} from $\bar{\mathcal{Z}}$ to construct the **FEC** tuples T_i in (6). For every tuple T_i , we evaluate the **FEC** using (2) and compute $n_{\text{sf},i}$ in (5) using the mapping in (8). Finally, the set $\bar{\mathcal{F}}$ includes all the elements $n_{\text{sf},i}$ as in (9).

C. Vision-based Pose Adaptation (VPA) Formulation

The **VPA** has four main stages as shown in Fig. 2(C). First, *heightmap extraction* that is similar to the **VFA**. Second, *pose evaluation* where we compute $\bar{\mathcal{F}}$. Third, *function approximation* where we estimate $\hat{\mathcal{F}}$ from $\bar{\mathcal{F}}$. Fourth, *pose optimization* where the optimal body pose is computed.

Heightmap Extraction. We extract one heightmap H_{vpa} per leg that is centered around the projection of the leg's hip location in the terrain map ($\text{proj.}(p_h)$ instead of p_n).

Pose Evaluation. After extracting the heightmaps, we compute $\bar{\mathcal{F}}$ from the mapping in (8) of the pose evaluation. In the pose evaluation, the **FEC** are evaluated for all hip heights in $\bar{\mathcal{Z}}$ given the input tuple T_{vpa} as shown in Fig. 3.

Function Approximation. In this stage, we estimate the continuous function $\hat{\mathcal{F}}$ from $\bar{\mathcal{F}}$, as explained in Remark 4. This is done by training a parameterized model of the inputs $T_i \in \bar{\mathcal{T}}$ and the outputs $n_{\text{sf},i} \in \bar{\mathcal{F}}$. The result is the function (model) $\hat{\mathcal{F}}$ that is parameterized by the model parameters w . The function approximation is detailed later in this section.

Pose Optimization. Evaluating the **FEC** and approximating it with the function $\hat{\mathcal{F}}$, introduces a metric that represents the possible number of safe footholds for every leg. Based on this, the goal of the pose optimizer is to find the optimal pose that will maximize the number of safe footholds for every leg (maximize $\hat{\mathcal{F}}$) while ensuring robustness. The pose optimizer is detailed later in this section.

Remark 5: Similar to Remark 3, one can directly apply the exact evaluation $g_{\text{vpa}}(T_{\text{vpa}})$ for a given T_{vpa} . Yet, since this is computationally expensive, we rely on approximating the evaluation $\hat{g}_{\text{vpa}}(T_{\text{vpa}})$ using a **CNN**. In fact, the learning part is applied to both the pose evaluation and the function approximation. This means that the pose optimization is running online, outside the **CNN**. The **CNN** architecture of the pose evaluation is explained in Appendix A.

D. Function Approximation

The goal of the function approximation is to approximate the set of safe footholds \mathcal{F} from the discrete set $\bar{\mathcal{F}}$ computed in the pose evaluation stage. This is done to provide the pose optimizer with a continuous function. Given a dataset $(\bar{\mathcal{Z}}, \bar{\mathcal{F}})$ of hip heights $z_{h_i} \in \bar{\mathcal{Z}}$ and number of safe footholds $n_{\text{sf},i} \in \bar{\mathcal{F}}$, the function approximation estimates a function $\hat{\mathcal{F}}(z_{h_i}, w)$ that is parameterized by the weights w . Once the weights w are computed, the function estimate $\hat{\mathcal{F}}(z_{h_i}, w)$ is then reconstructed and sent to the pose optimizer.

It is important to choose a function $\hat{\mathcal{F}}$ that can accurately represent the nature of the number of safe footholds. The number of safe footholds approaches zero when the hip heights approach 0 or ∞ . Thus, we want a function that fades to zero at the extremes (Gaussian-like functions), and captures any asymmetry or flatness in the distribution. Hence, we use radial basis functions of Gaussians. With that in mind, we are looking for the weights w

$$w = \arg \min S(w) \quad (10)$$

that minimize the cost $S(w)$

$$S(w) = \sum_{i=1}^{N_h} (n_{sf,i} - \hat{\mathcal{F}}(z_{h_i}, w))^2 \quad (11)$$

which is the sum of the squared residuals of $n_{sf,i}$ and $\hat{\mathcal{F}}(z_{h_i}, w)$. N_h is the number of samples (the number of the finite set of hip heights). The function $\hat{\mathcal{F}}(z_{h_i}, w)$ is the regression model (the approximation of \mathcal{F}) that is parameterized by w . The function $\hat{\mathcal{F}}(z_{h_i}, w)$ is the weighted sum of the basis functions

$$\hat{\mathcal{F}}(z_{h_i}, w) = \sum_{e=1}^E w_e \cdot g(z_{h_i}, \Sigma_e, c_e) \quad (12)$$

where $w \in \mathbb{R}^E$, and E is the number of basis functions. The basis function is a radial basis function of Gaussian functions

$$g(z_{h_i}, \Sigma_e, c_e) = \exp(-0.5(z_{h_i} - c_e)^T \Sigma_e^{-1} (z_{h_i} - c_e)) \quad (13)$$

where Σ_e and c_e are the parameters of the Gaussian function. Since the function model in (12) is linear in the parameters, the weights of the function approximation can be solved analytically using least squares. In this work, we keep the parameters of the Gaussians (Σ and c) fixed. Hence, the function $\hat{\mathcal{F}}$ is only parameterized by w . For more information on regression with radial basis functions, please refer to [57] and Appendix B.

E. Pose Optimization

The pose optimizer finds the robot's body pose u that maximizes the number of safe footholds for all the legs. This is casted as a non-linear optimization problem. The notion of safe footholds is provided by the function $\hat{\mathcal{F}}(z_h, w)$ that maps a hip height z_h to a number of safe foothold n_{sf} , and is parameterized by w . Since the pose optimizer is solving for the body pose u , the function $\hat{\mathcal{F}}(z_h)$ should be encoded using the body pose rather than the hip heights ($\hat{\mathcal{F}} = \hat{\mathcal{F}}(z_h(u))$). This is done by estimating the hip height as a function of the body pose ($z_h = z_h(u)$) as shown in Appendix C.

F. Single-Horizon Pose Optimization

The pose optimization problem is formulated as

$$\underset{u=[z_b, \beta, \gamma]}{\text{maximize}} \quad \mathcal{C}(\hat{\mathcal{F}}_l(z_{h_l}(z_b, \beta, \gamma))) \quad \forall l \in N_l \quad (14)$$

$$\text{subject to} \quad u_{\min} \leq u \leq u_{\max} \quad (15)$$

$$\Delta u_{\min} \leq \Delta u \leq \Delta u_{\max} \quad (16)$$

where $u = [z_b, \beta, \gamma] \in \mathbb{R}^3$ are the decision variables (robot body pose) consisting of the robot height, roll and pitch, respectively, \mathcal{C} is the cost function, $\hat{\mathcal{F}}_l$ is $\hat{\mathcal{F}}$ for every leg l where $N_l = 4$ is the number of legs, $z_{h_l} \in \mathbb{R}$ is the hip height of the leg l , and u_{\min} and u_{\max} are the lower and upper bounds of the decision variables, respectively. $\Delta u = u - u_{k-1}$ is the numerical difference of u where u_{k-1} is the output of u at the previous instant, and Δu_{\min} and Δu_{\max} are the lower and upper bounds of Δu , respectively. We can re-write (16) as

$$\Delta u_{\min} + u_{k-1} \leq u \leq \Delta u_{\max} + u_{k-1}. \quad (17)$$

The cost function in (14) maximizes $\hat{\mathcal{F}}$ for all of the legs. We designed several types of cost functions as detailed next. The constraints in (15) and (16) ensure that the decision variables and their variations are bounded.

G. Cost Functions

A standard cost function can be the sum of the squares of $\hat{\mathcal{F}}_l$ for all of the legs

$$\mathcal{C}_{\text{sum}} = \sum_{l=1}^{N_l=4} \|\hat{\mathcal{F}}_l(z_{h_l})\|_Q^2 \quad (18)$$

where another option could be the product of the squares of $\hat{\mathcal{F}}_l$ for all of the legs

$$\mathcal{C}_{\text{prod}} = \prod_{l=1}^{N_l=4} \|\hat{\mathcal{F}}_l(z_{h_l})\|_Q^2. \quad (19)$$

The key difference between an additive cost \mathcal{C}_{sum} and a multiplicative cost $\mathcal{C}_{\text{prod}}$ is that the latter puts equal weighting for each $\hat{\mathcal{F}}_l$. This is important since we do not want the optimizer to find a pose that maximizes $\hat{\mathcal{F}}$ for one leg while compromising the other leg(s). One can also define the cost

$$\mathcal{C}_{\text{int}} = \sum_{l=1}^{N_l=4} \left\| \int_{z_{h_l}-m}^{z_{h_l}+m} \hat{\mathcal{F}}_l(z_{h_l}) dz_{h_l} \right\|_Q^2 \quad (20)$$

which is the *sum of squared integrals* that can be numerically approximated as

$$\int_{z_{h_l}-m}^{z_{h_l}+m} \hat{\mathcal{F}}_l(z_{h_l}) dz_{h_l} \approx m \cdot (\hat{\mathcal{F}}_l(z_{h_l}-m) + \hat{\mathcal{F}}_l(z_{h_l}+m)) \quad (21)$$

yielding

$$\mathcal{C}_{\text{int}} = \sum_{l=1}^{N_l=4} \|m \cdot (\hat{\mathcal{F}}_l(z_{h_l}-m) + \hat{\mathcal{F}}_l(z_{h_l}+m))\|_Q^2. \quad (22)$$

In this cost option, we do not find the pose that maximizes $\hat{\mathcal{F}}$. Instead, we want to find the pose that maximizes the area around $\hat{\mathcal{F}}$ that is defined by the margin m . Using \mathcal{C}_{int} is important since it adds robustness in case there is any error in the pose tracking during execution. Because of possible tracking errors during execution, the robot might end up in the pose $u^* \pm m$ instead of u^* . If we use \mathcal{C}_{int} as a cost function, the optimizer will find poses that maximizes the number of safe footholds not just for u^* but within a vicinity of m . More details on the use of \mathcal{C}_{int} as a cost function in the pose optimization of the VPA can be found in Appendix D.

H. Receding-Horizon Pose Optimization

Adapting the robot's pose during dynamic locomotion requires reasoning about what is ahead of the robot: the robot should not just consider its current state but also future ones. For that, we extend the pose optimizer to consider the current and future states of the robot in a receding horizon manner. To formulate the receding horizon pose optimizer, instead of considering $\hat{\mathcal{F}}_l \forall l \in N_l$ in the single horizon case, the pose optimizer will consider $\hat{\mathcal{F}}_{l,j} \forall l \in N_l, j \in N_h$ where N_h is the receding horizon number. We compute $\hat{\mathcal{F}}_{l,j}$ in the same way explained in the pose evaluation stage. More details on computing $\hat{\mathcal{F}}_{l,j}$ can be found in Appendix E.

The receding horizon pose optimization problem is

$$\begin{aligned} & \underset{u=[u_1^T, \dots, u_{N_h}^T]}{\text{maximize}} && \sum_{j=1}^{N_h} \mathcal{C}_j(\hat{\mathcal{F}}_{l,j}(z_{h_{l,j}}(u_j))) \\ & + \sum_{j=1}^{N_h-1} \|u_j - u_{j+1}\| \\ & \forall l \in N_l, j \in N_h \end{aligned} \quad (23)$$

$$\text{subject to} \quad u_{\min} \leq u \leq u_{\max} \quad (24)$$

$$\Delta u_{\min} \leq \Delta u \leq \Delta u_{\max} \quad (25)$$

where $u = [u_1^T, \dots, u_j^T, \dots, u_{N_h}^T] \in \mathbb{R}^{3N_h}$ are the decision variables during the entire receding horizon N_h . Each variable $u_j = [z_{b,j}, \beta_j, \gamma_j] \in \mathbb{R}^3$ is the optimal pose of the horizon j .

The first term in (23) is the sum of the cost functions \mathcal{C}_j during the entire horizon ($\forall j \in N_h$). The cost \mathcal{C}_j can be any of the aforementioned cost functions. The second term in (23) penalizes the deviation between two consecutive optimal poses within the receding horizon (u_j and u_{j+1}). The second term is added so that each optimal pose u_j is also taking into account the optimal pose of the upcoming sequence u_{j+1} (to connect the solutions in a smooth way). Similar to the single horizon pose optimizer, u_{\min} and u_{\max} are the lower and upper bounds of the decision variables, respectively. Furthermore, Δu denotes the numerical difference of u , while Δu_{\min} and Δu_{\max} are the lower and upper bounds of Δu , respectively. Note that the constraints of the single horizon and the receding horizon are of different dimensions.

V. SYSTEM OVERVIEW

Our locomotion framework that is shown in Fig. 2(D) is based on the **Reactive Controller Framework (RCF)** [56]. **ViTAL** complements the RCF with an exteroceptive terrain-aware layer composed of the **VFA** and the **VPA**. **ViTAL** takes the robot states, the terrain map and user commands as inputs, and sends out the selected footholds and body pose to the RCF (perceptive) layer. The RCF takes the robot states and the references from **ViTAL**, and uses them inside a motion generation and a motion control block. The motion generation block generates the trajectories of the leg and the body, and adjusts them with the reflexes from [56], [58]. The legs and body references from the motion generation block are sent to the motion control block. The motion control block consists of a **Whole-Body Controller (WBC)** [59] that generates desired

torques that are tracked via a low-level torque controller [60], and sent to the robot's joints. The framework also includes a state estimation block that feeds back the robot states to each of the aforementioned layers [61]. More implementation details on **ViTAL** and the entire framework is in Appendix F.

We demonstrate **ViTAL** on the 90 kg **HyQ** and the 140 kg **HyQReal** quadruped robots. Each leg of the two robots has 3 degrees of freedom (3 actuated joints). The torques and angles of the 12 joints of both robots are directly measured. The bodies of **HyQ** and **HyQReal** have a tactical-grade **Inertial Measurement Unit (IMU)** (KVH 1775). More information on **HyQ** and **HyQReal** can be found in [62], and [3] respectively.

We noticed a significant drift in the states of the robots in experiment. To tackle this issue, the state estimator fused the data from a motion capture system and the **IMU**. This reduced the drift in the base states of the robots albeit not eliminating it completely. Improving the state estimation is an ongoing work and is out of the scope of this article. We used the grid map interface [63] to get the terrain map in simulation. Due to the issues with state estimation on the real robots, we constructed the grid map before the experiments, and used the motion capture system to locate the map with respect to the robot.

VI. RESULTS

We evaluate **ViTAL** on **HyQ** and **HyQReal**. We consider all the **FEC** mentioned earlier for the **VFA** and the **VPA**. We use the receding horizon pose optimizer of (25) and the sum of squared integral of (22). We choose stair climbing as an application for **ViTAL**. Climbing stairs is challenging for **HyQ** due to its limited leg workspace in the sagittal plane. Videos associated with the upcoming results can be found in the supplementary materials and [64]. Finally, an analysis of the accuracy of the **CNNs** and the computational time of **ViTAL** can be found in Appendix G and Appendix H, respectively.

A. Climbing Stairs (Simulation)

We carried out multiple simulations where **HyQ** is climbing the stairs shown in Fig. 4. Each step has a rise of 10 cm, and a go of 25 cm. **HyQ** is commanded to trot with a desired forward velocity of 0.2 m/s using the **VPA** and the **VFA**. Figure 4 shows screenshots of one simulation run, and Video 1 shows three simulation runs.

Figure 4 shows the ability of the **VPA** in adapting the robot pose to increase the chances of the legs to succeed in finding a safe foothold. In Fig. 4(B), **HyQ** raised its body and pitched upwards so that the front hips are raised to increase the workspace of the front legs when stepping up. In Fig. 4(C), **HyQ** raised its body and pitched downwards so that the hind hips are raised. This is done for two reasons. First, to have a larger clearance between the hind legs and the obstacle, and thus avoiding leg collision with the edge of the stairs. Second, to increase the workspace of the hind legs when stepping up, and thus avoiding reaching the workspace limits and collisions along the foot swing trajectory. In Fig. 4(D), **HyQ** lowered its body and pitched downwards so that the front hips are lowered. This is done for two reasons: First, to increase the workspace of the front legs when stepping down, and thus

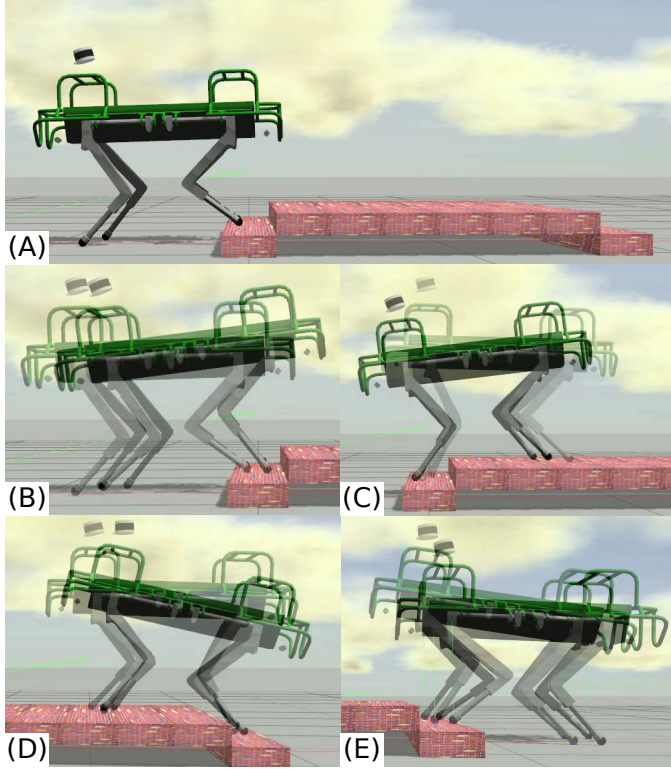


Fig. 4. **HyQ** climbing stairs in simulation. (A) The full scenario. (B) The robot pitches up to allow for safe footholds for the front legs. (C) The robot lifts up the hind hips to avoid hind leg collisions with the step. (D) The robot pitches down to allow for safe footholds for the front legs. (E) The robot lowers the hind hips to allow for safe footholds for the legs when stepping down.

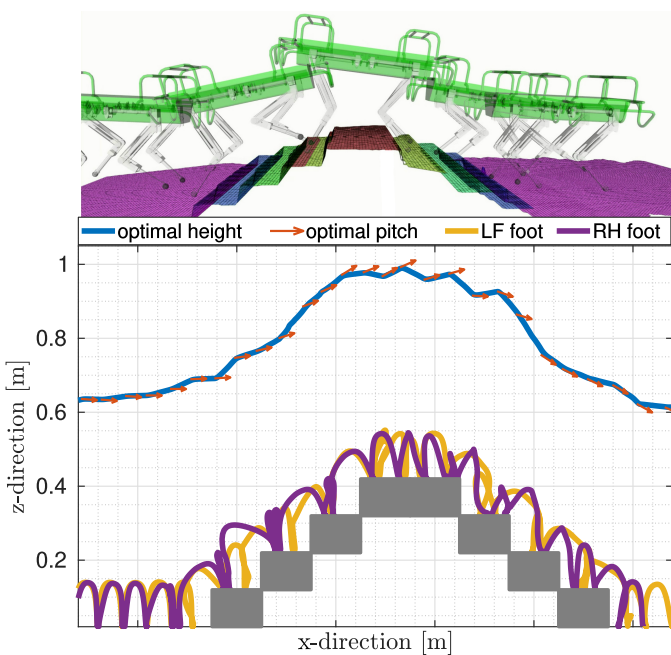


Fig. 5. Climbing Stairs: A More Complex Scenario. Top: Overlayed screenshots of **HyQ** climbing stairs. Bottom: the optimal height and corresponding pitch (presented by the arrows) and the foot trajectories of **LF** and **RH** legs.

avoiding reaching the workspace limits. Second, to have a larger clearance between the front legs and the obstacle, and thus avoiding leg collisions. In Fig. 4(E), **HyQ** lowered its hind hips to increase the hind legs' workspace when stepping down.

Throughout these simulations, the robot continuously adapted its body pose and its feet to find the best trade-off between increasing the kinematic feasibility, and avoiding trajectory and leg collision. This can be seen in Video 1 where the robot's legs and the corresponding feet trajectories never collided with the terrain. The robot took multiple steps around the same foot location before stepping over an obstacle. The reason behind this is that the robot waited for the **VPA** to change the pose and allow for safe footholds, and then the **VFA** took the decision of stepping over the obstacle.

We carried out another scenario where **HyQ** is climbing the stairs setup in Fig. 5 where each step has a rise of 10 cm, and a go of 25 cm. **HyQ** is commanded to trot with a desired forward velocity of 0.2m/s using **ViTAL**. The results are reported in Fig. 5 and Video 2. Figure 5 shows the robot's height and pitch based on the **VPA**, and the corresponding feet trajectories of the **LF** leg and the **RH** leg based on the **VFA**. **HyQ**'s behavior was similar to the previous section: it accomplished the task without collisions or reaching workspace limits.

B. Climbing Stairs (Experiments)

To validate **ViTAL** in experiments, we created three sets of experiments using the setups shown in Fig. 1. Each step has a rise of 10 cm, and a go of 28 cm.

In the first set of experiments, **HyQ** is commanded to crawl over the setups in Fig. 1(A,B) with a desired forward velocity of 0.1 m/s using the **VPA** and the **VFA**. Figures 6(A-F) show screenshots of one trial. Video 3 shows **HyQ** climbing back and forth the setup in Fig. 1(B) five times. Video 4 shows **HyQ** climbing the Fig. 1(A) setup, which is reported in Fig. 7. Figure 7 shows the robot's height and pitch based on the **VPA**, and the corresponding feet trajectories of the **Left-Front (LF)** leg and the **Right-Hind (RH)** leg based on the **VFA**. This set of experiments confirms that **ViTAL** is effective on the real platform. The robot managed to accomplish the task without collisions or reaching workspace limits.

In the second set of experiments, **HyQ** is commanded to trot over the setup in Fig. 1(B) with a desired forward velocity of 0.25 m/s using the **VPA** and the **VFA**. Figures 6(G-L) show separate screenshots of this trial. Video 5 shows three trials of **HyQ** climbing the same setup. This set of experiments shows that **ViTAL** can handle different gaits.

Finally, in the third set of experiments, **HyQReal** is commanded to crawl over the setup in Fig. 1(C) with a desired forward velocity of 0.2 m/s using the **VPA** and the **VFA**. The results are reported in Fig. 6(M-R) that show screenshots of this trial. Video 6 shows **HyQReal** climbing this stair setup (Fig. 1(C)). This set of experiments shows that **ViTAL** can work on different legged platforms.

The tracking performance of these three sets of experiments are shown in Table I. The table shows the mean absolute tracking errors of the body pitch β and height z_b of **HyQ** and **HyQReal**.

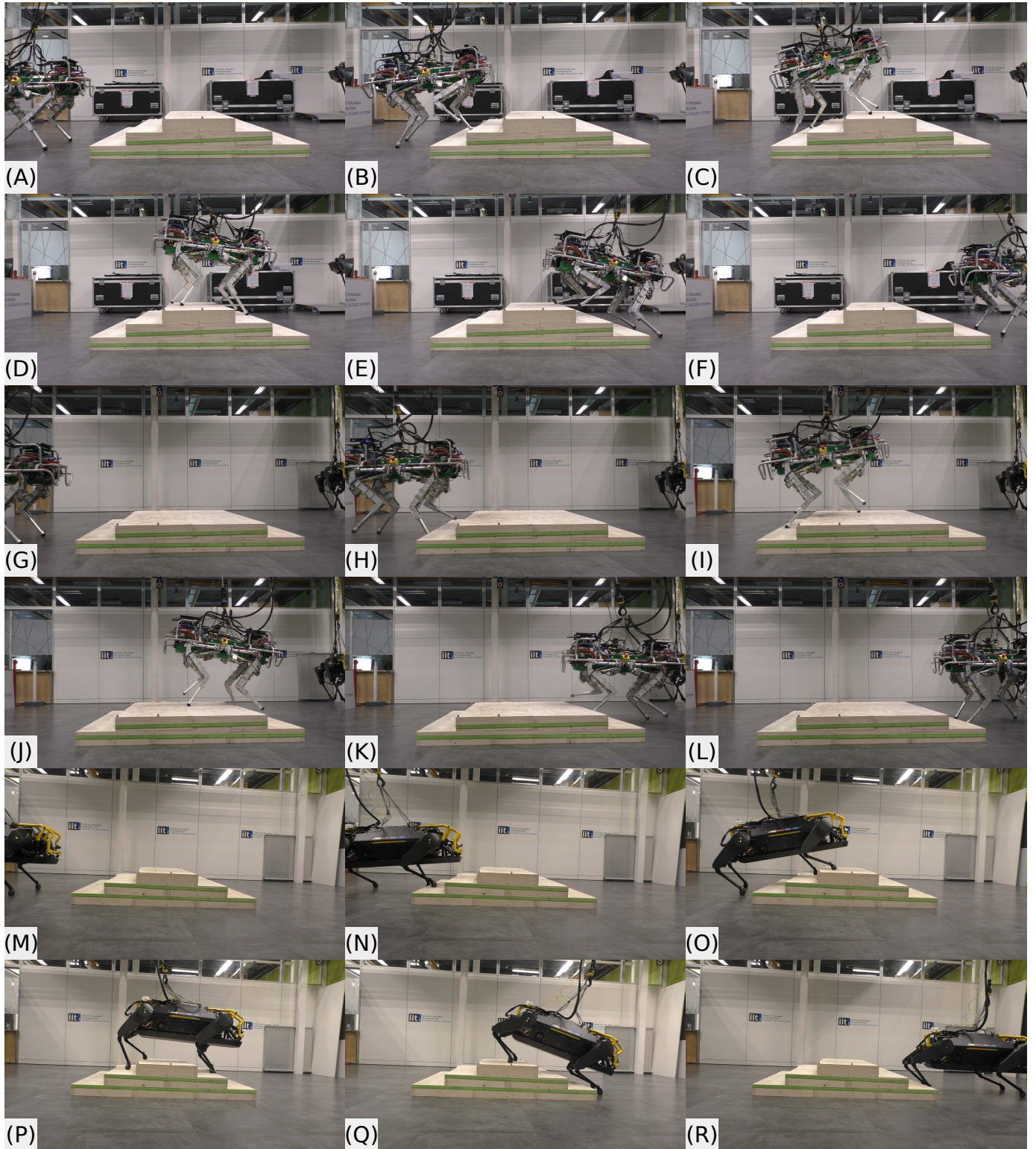


Fig. 6. **HyQ** and **HyQReal** climbing stairs in experiment. (A-F) **HyQ** crawling over with 0.1 m/s commanded forward velocity. (G-L) **HyQ** trotting over with 0.25 m/s commanded forward velocity. (M-R) **HyQReal** crawling over with 0.2 m/s commanded forward velocity.

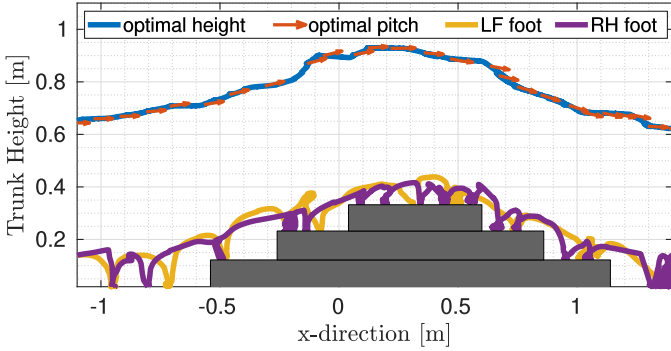


Fig. 7. **HyQ** climbing stairs in experiment. The figure shows the optimal height and corresponding pitch (presented by the arrows) based on the **VPA**, and the foot trajectories of the **LF** and **RH** legs based on the **VFA**.

TABLE I

MEAN ABSOLUTE TRACKING ERRORS OF THE BODY PITCH β AND HEIGHT z_b OF **HyQ** & **HyQReal** USING **VITAL** IN THE EXPERIMENTS DETAILED IN SECTION VI-B AND IN FIG. 1.

Description	β [deg]	z_b [cm]
Exp. (A): HyQ crawling at 0.1 m/s	1.0	1.5
Exp. (B): HyQ trotting at 0.2 m/s	1.0	2.3
Exp. (C): HyQReal crawling at 0.2 m/s	1.0	4.2

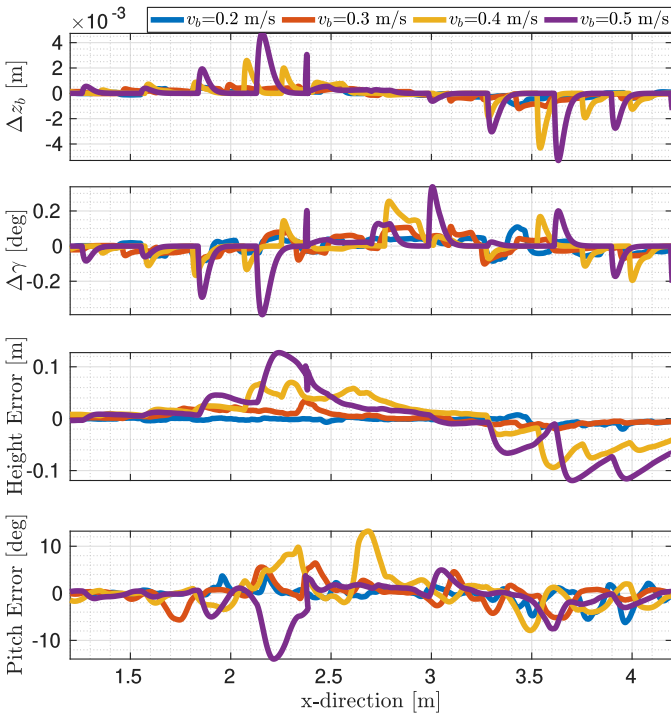


Fig. 8. **HyQ**'s performance using **VITAL** under different commanded velocities. The top two plots show the numerical difference of the body height and pitch (Δz_b and $\Delta \gamma$), and the bottom two plots show the tracking errors of the body height and pitch.

C. Climbing Stairs with Different Forward Velocities

We evaluate the performance of **HyQ** under different commanded velocities using **VITAL**. We carried out a series of simulations using the stairs setup shown in Fig. 5. **HyQ** is commanded to trot at four different forward velocities: 0.2 m/s,

TABLE II
MEAN ABSOLUTE TRACKING ERRORS OF THE BODY PITCH β AND HEIGHT z_b OF **HyQ** USING **VITAL** IN SIMULATION WITH DIFFERENT FORWARD VELOCITIES AS DETAILED IN SECTION VI-C AND FIG. 8.

Description	β [deg]	z_b [cm]
Sim. (A): HyQ trotting at 0.2 m/s	0.7	0.3
Sim. (B): HyQ trotting at 0.3 m/s	1.1	0.7
Sim. (C): HyQ trotting at 0.4 m/s	2.3	2.6
Sim. (D): HyQ trotting at 0.5 m/s	1.6	3.8

0.3 m/s, 0.4 m/s, and 0.5 m/s. The results are reported in Fig. 8 and in Video 7. Additionally, the tracking performance of these series of simulations at the four different forward velocities are shown in Table II. The table shows the mean absolute tracking errors of the body pitch β and height z_b of **HyQ** at the corresponding commanded forward velocity. Figure 8 shows the numerical differences Δz_b and $\Delta \gamma$, and the tracking errors of the body height and pitch, respectively.

HyQ was able to climb the stairs terrain under different commanded velocities. However, as the commanded velocity increases, **HyQ** started having faster (abrupt) changes in the body pose as shown in the top two plots of Fig. 8. As a result, the height and pitch tracking errors increase proportionally to the commanded speed as shown in the bottom two plots of Fig. 8. This can also be seen in Table II where the mean absolute tracking errors of the pitch and height increase proportionally to the commanded speed.

Similarly to **HyQ**, we evaluate **VITAL** on **HyQReal** and commanded it to trot with five different forward velocities: 0.2 m/s, 0.3 m/s, 0.4 m/s, 0.5 m/s, and 0.75 m/s. We report this simulation in Video 8 where we show that **VITAL** is robot independent. Yet, since the workspace of **HyQReal** is larger than **HyQ**, this scenario was more feasible to traverse for **HyQReal**. Thus, **HyQReal** was able to reach a higher commanded velocity than the ones reported for **HyQ**.

D. Comparing the VPA with a Baseline (Experiments)

We compare the **VPA** with another vision-based pose adaptation strategy: the **Terrain-Based Body Reference (TBR)** [38]. The **TBR** generates pose references based on the footholds selected by the **VFA**. The **TBR** fits a plane that passes through the given selected footholds, and sets the orientation of this plane as a body orientation reference to the robot. The elevation reference of the **TBR** is a constant distance from the center of the approximated plane that passes through the selected footholds. We chose the **TBR** instead of an optimization-based strategy since the latter does not provide references that are fast enough with respect to the **VPA**.

Using the stairs setup in Fig. 1(A), we conducted six experimental trials: three with the **VPA** and three with the **TBR**. All trials were with the **VPA**. In all trials, **HyQ** is commanded to crawl with a desired forward velocity of 0.1 m/s. The results are reported in Fig. 9 and Video 9. Figure 9(A) shows the number of safe footholds corresponding to the robot pose from the **VPA** and the **TBR**. The robot height and pitch tracking errors are shown in Fig. 9(B,C), respectively.

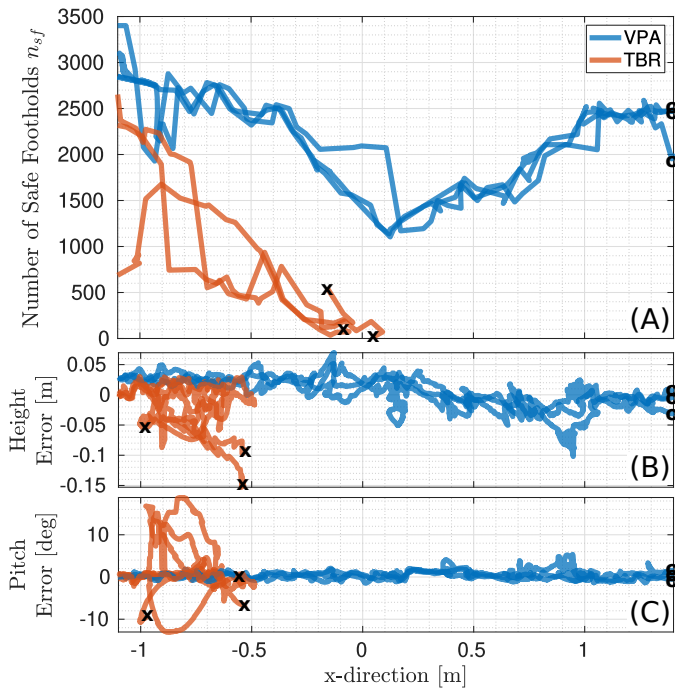


Fig. 9. The difference between the **VPA** and the **TBR** in six experiments (3 each). (A) The number of safe footholds corresponding to the robot pose. (B,C) The body height and pitch tracking errors, respectively. Circles (\circ) and crosses (\times) are successful and failed trials, respectively. Unlike the **VPA**, the **TBR** failed to climb the stairs because the **TBR** resulted in almost no safe footholds for the four legs to reach.

As shown in Video 9, **HyQ** failed to climb the stairs with the **TBR**, while it succeeded with the **VPA**. This is because, unlike the **VPA**, the **TBR** does not aim to put the robot in a pose that maximizes the chances of the legs to succeed in finding safe footholds. As shown in Fig. 9(A), the number of safe footholds from using the **TBR** was below the ones from using the **VPA**. During critical periods when the robot was around 0 m in the x-direction, the number of safe footholds from using the **TBR** almost reached zero. The low number of safe footholds for the **TBR** compared to the **VPA** is reflected in the tracking of the robot height and pitch as shown in Fig. 9(B,C) where the tracking errors from the **TBR** were higher than the **VPA**.

The difference between the **VPA** and the **TBR** can be further explained in Video 9. When the **TBR** is used, the robot is adapting its pose *given* the selected foothold. But, if the selected foothold is not reached, or if there is a high tracking error, the robot reaches a body pose that results in a smaller number of safe footholds. Thus, the feet end up colliding with the terrain and hence the robot falls. On the other hand, the **VPA** is able to put the robot in a pose that maximizes the number of safe footholds. As a result, the feet found alternative safe footholds to select from, which resulted in no collision, and succeeded in climbing the stairs. The **VPA** optimizes for the number of safe footholds. Thus, if there is a variation around the optimal pose (tracking error), the **VFA** still finds more footholds to step on, which is not the case with the **TBR**.

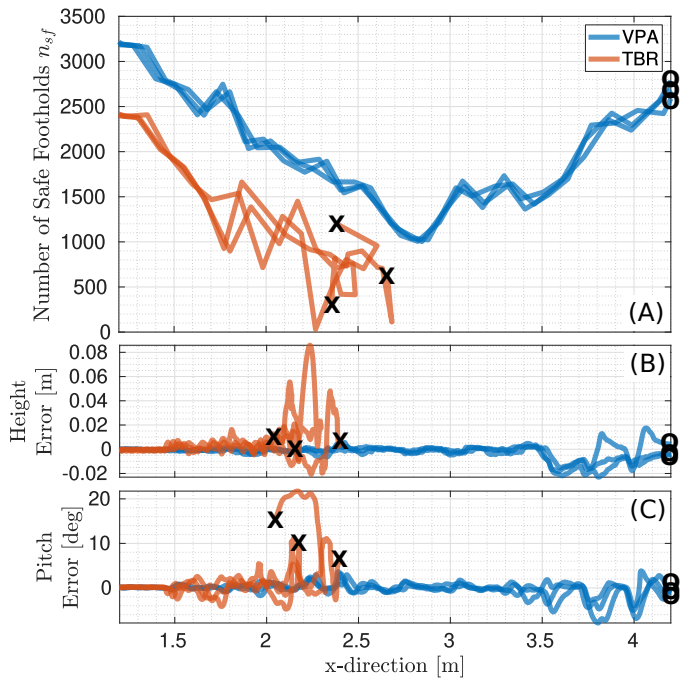


Fig. 10. The difference between the **VPA** and the **TBR** in six simulations (3 each). (A) The number of safe footholds corresponding to the robot pose. (B,C) The body height and pitch tracking errors, respectively. Circles (\circ) and crosses (\times) are successful and failed trials, respectively. Unlike the **VPA**, the **TBR** failed to climb the stairs because the **TBR** resulted in almost no safe footholds for the four legs to reach.

E. Comparing the **VPA** with a Baseline (Simulation)

Similar to experiments, and using the stairs setup in Fig. 5, we compare the **VPA** with the **TBR**. We conducted six simulations: three with the **VPA** and three with the **TBR**. All trials were with the **VFA**. In all trials, **HyQ** is commanded to trot with a 0.2m/s desired forward velocity. The results are reported in Fig. 10 and Video 10. Figure 10(A) shows the number of safe footholds corresponding to the robot pose from the **VPA**, and the **TBR**. The tracking errors of the robot height and pitch are shown in Fig. 10(B,C), respectively. These trials show that **HyQ** failed to climb the stairs using the **TBR**, while it succeeded using the **VPA**.

F. Climbing Stairs with Gaps

We show **HyQ**'s capabilities of climbing stairs with gaps using **ViTAL**, and we compare the **VPA** with the **TBR**. In this scenario, **HyQ** is commanded to trot at 0.4 m/s. Figure 11(A) shows overlaid screenshots of the simulation and the used setup. Figure 11(B) shows the robot's height and pitch based on the **VPA**, and the corresponding feet trajectories of the **LF** leg and the **RH** leg based on the **VFA**, and Fig. 11(C) shows the number of safe footholds using the **VPA** and the **TBR**. Because of **ViTAL**, **HyQ** was able to climb the stairs with gaps while continuously adapting its pose and feet. Furthermore, the number of safe footholds from using the **TBR** is always lower than from using the **VPA**, which shows that indeed the **VPA** outperforms the **TBR**. Video 11 shows the output of this simulation using **ViTAL**.

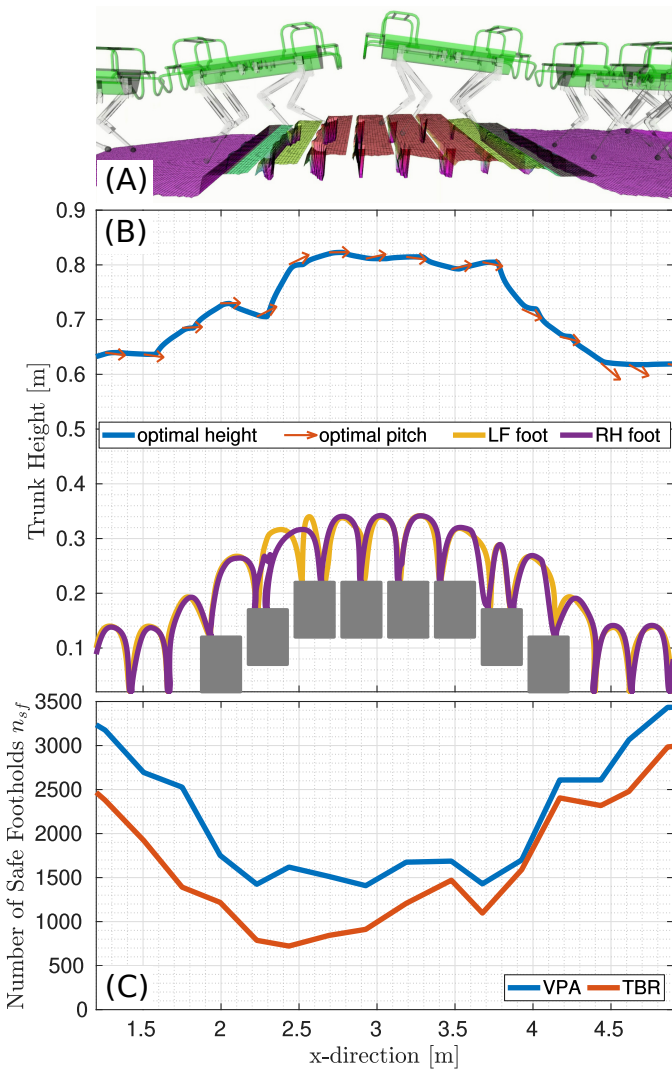


Fig. 11. **HyQ** climbing gapped stairs. (A) Screenshots of **HyQ** climbing the setup. (B) The robot’s height and pitch based on the **VPA**, and the corresponding feet trajectories of the **LF** and **RH** legs based on the **VFA**. (C) The number of safe footholds using the **VPA** and the **TBR**.

G. Pose Optimization: Single vs. Receding Horizons

To analyze the differences between the receding horizon and the single horizon in pose optimization, we use the stairs setup in Fig. 5 with a commanded forward velocity of 0.4 m/s, and report the outcome in Fig. 12 and Video 12. The main advantage of using a receding horizon instead of a single horizon is that the pose optimization can consider future decisions. Thus, if the robot is trotting at higher velocities, the pose optimizer can adapt the robot’s pose before hand. This can result in a better adaptation strategy with less variations in the generated optimal pose. Thus, we analyze the two approaches by taking a look at the variations in the body pose

$$\dot{z}_b = \frac{\Delta z_b}{\Delta x_b}, \quad \text{and} \quad \dot{\gamma} = \frac{\Delta \gamma}{\Delta x_b} \quad (26)$$

where \dot{z}_b and $\dot{\gamma}$ are the numerical differences (variations) of the robot height z_b and pitch γ with respect to the robot forward position x_b , respectively.

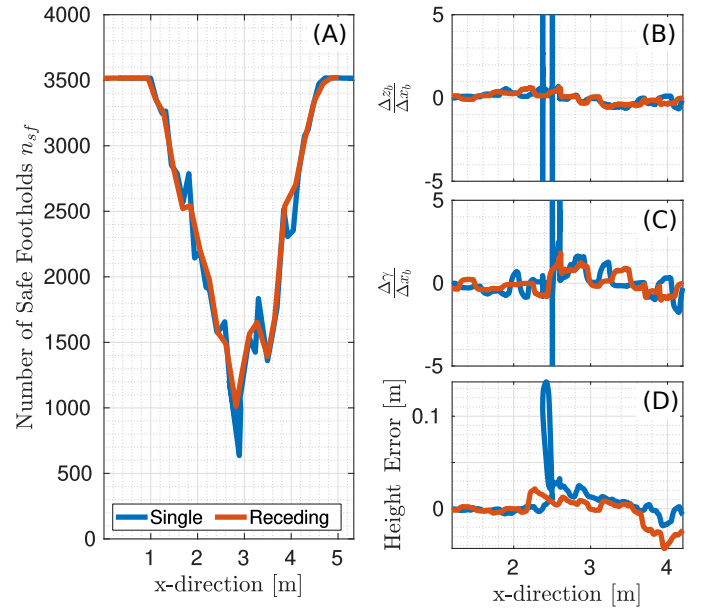


Fig. 12. Pose Optimization: Single vs. Receding Horizons. (A) The number of safe footholds. (B) Variation (numerical difference) of the robot’s height. (C) Variation (numerical difference) of the robot’s pitch. (D) The tracking error of the robot’s height.

Figure 12 reports the differences between the two cases. The number of safe footholds is shown in Fig. 12(A). The variations in \dot{z}_b and $\dot{\gamma}$ are shown in Fig. 12(B,C), respectively. Finally, the tracking error of the robot’s height is shown in Fig. 12(D). As shown in Figure 12 the receding horizon resulted in less variations in the body pose compared to the single horizon. This resulted in a smaller tracking error for the receding horizon in the body height, which resulted in slightly larger number of safe footholds. All in all, the receding horizon reduces variations in the desired trajectories which improves the trajectory tracking response.

The differences between the receding and single horizon in the pose optimization can also be noticed in Video 12. In the case of a single horizon, the robot was struggling while climbing up the stairs but was able to recover and accomplish the task. However, using the receding horizon, the robot was able to adapt its pose in time, and thus resulting in safer footholds that allowed the robot to accomplish the task.

H. Pose Optimization: \mathcal{C}_{sum} vs. \mathcal{C}_{int}

To analyze the differences between \mathcal{C}_{sum} and \mathcal{C}_{int} in the pose optimization, we use the stairs setup in Fig. 5 with a commanded forward velocity of 0.4 m/s, and report the outcome in Fig. 13. The main advantage of using \mathcal{C}_{int} over \mathcal{C}_{sum} is that \mathcal{C}_{int} will result in a pose that does not just maximize the number of safe footholds for all of the legs, but also ensures that the number of safe footholds of the poses around the optimal pose is still high. To compare the two cost functions, we take a look at the number of safe footholds. In particular, we evaluate the number of safe footholds corresponding to the optimal pose, and the poses around it with a margin of $m = 0.025$ m. Thus, in Fig. 13, we plot the envelope (shaded area) between $\hat{\mathcal{F}}(u^* + m)$ and

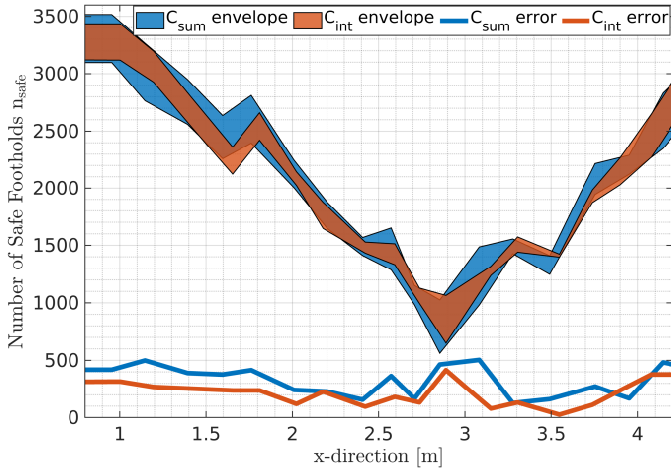


Fig. 13. Pose Optimization: C_{sum} vs. C_{int} . The shaded areas are the envelopes of the number of safe footholds. The lines are the thicknesses (errors) between these envelopes.

$\hat{\mathcal{F}}(u^* - m)$ for both cases, and the thickness between these envelopes which we refer to as error

$$\text{error} = |\hat{\mathcal{F}}(u^* + m) - \hat{\mathcal{F}}(u^* - m)|. \quad (27)$$

As shown in Fig. 13 the envelope of the number of safe footholds resulting from C_{int} is almost always encapsulated by C_{sum} . The thickness (error) of the number of safe footholds resulting from using C_{int} is always smaller than C_{sum} . This means that any variation of m in the optimal pose will be less critical if C_{int} is used compared to C_{sum} .

I. Locomotion over Rough Terrain

We evaluate the performance of **HyQ** in traversing rough terrain as shown in Fig. 14(A,B) and in Video 13. We conducted two simulations: one with **ViTAL** and thus with exteroceptive and proprioceptive reactions (Fig. 14(A)), and another without **ViTAL** and thus only with proprioceptive reactions (Fig. 14(B)). **HyQ** was commanded to traverse the rough terrain with a forward velocity of 0.2 m/s. No hyper parameters re-tuning, or **CNNs** re-training were needed.

As shown in Video 13, **HyQ** was able to successfully traverse the terrain in both cases. With **ViTAL**, **HyQ** collided less with the terrain and continuously adapted its footholds over the small cobblestones. Without **ViTAL**, **HyQ** traversed the rough terrain, yet, with significantly more effort. Additionally, without **ViTAL**, **HyQ** continuously collided with the terrain, and in some incidents, the feet got stuck. For this reason, we had to re-tune the gait parameters, and increase the step height to reduce these incidents. The robot's feet also kept slipping since the feet were always close to edges and corners.

J. Climbing Stairs with Different Commands

Instead of commanding only forward velocities as in the previous sections, we command **HyQ** to climb the stairs with **ViTAL** while yawing (commanding the yaw rate) as shown in Video 14 and Fig. 14(C,D), and to climb stairs laterally as shown in Video 15 and Fig. 14(E,F). Climbing

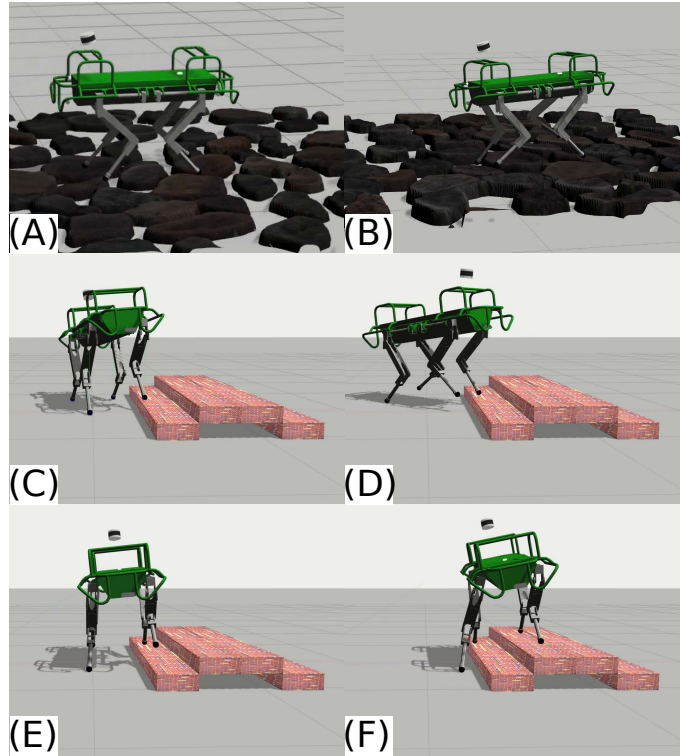


Fig. 14. **HyQ** traversing rough terrain and climbing stairs sideways. (A,B) **HyQ** traversing rough terrain with and without **ViTAL**, respectively. (C,D) **HyQ** climbing stairs while yawing (commanding the yaw rate) using **ViTAL**. (E,F) **HyQ** climbing stairs sideways using **ViTAL**.

stairs sideways is more challenging than facing the stairs since the range of motion of the robot's roll orientation is more restricted versus the pitch orientation. That said, because of **ViTAL**, **HyQ** was still able to climb these stairs in both cases as shown in Video 14 and Video 15.

VII. CONCLUSION

We presented **ViTAL** which is an online vision-based locomotion planning strategy. **ViTAL** consists of the **VPA** for pose adaptation, and the **VFA** for foothold selection. The **VPA** introduces a different paradigm to current state-of-the-art pose adaptation strategies. The **VPA** finds body poses that maximize the chances of the legs to succeed in reaching safe footholds. This notion of success emerges from the robot's skills. These skills are encapsulated in the **FEC** that include (but are not limited to) the terrain roughness, kinematic feasibility, leg collision, and foot trajectory collision. The **VFA** is a foothold selection algorithm that continuously adapts the robot's trajectory based on the **FEC**. The **VFA** algorithm of this work extends our previous work in [38], [49] as well as the state of the art [37], [46]. Since the computation of the **FEC** is usually expensive, we rely on approximating these criteria with **CNNs**.

The robot's skills and the notion of success provided by the **FEC** allowed the **VPA** to generate body poses that maximize the chances of success in reaching safe footholds. This resulted in body poses that are aware of the terrain and aware of what the robot and its legs can do. For that reason, the **VPA** was able

to generate body poses that give a better chance for the **VFA** to select safe footholds. As a result, because of **ViTAL**, **HyQ** and **HyQReal** were able to traverse multiple terrains with various forward velocities and different gaits without colliding or reaching workspace limits. The terrains included stairs, gaps, and rough terrains, and the commanded velocities varied from 0.2 m/s to 0.75 m/s. The **VPA** outperformed other strategies for pose adaptation. We compared **VPA** with the **TBR** which is another vision based pose adaptation strategy, and showed that indeed the **VPA** puts the robot in a pose that provides the feet with higher number of safe footholds. Because of this, the **VPA** made our robots succeed in various scenarios where the **TBR** failed.

VIII. LIMITATIONS AND FUTURE WORK

One issue that we faced during experiment was in tracking the motion of the robot, especially for **HyQReal**. We were using a **WBC** for motion tracking. We believe that the motion tracking and our strategy can be improved by using a **Model Predictive Control (MPC)** alongside the **WBC**. Similarly, instead of using a model-based controller (**MPC** or **WBC**), we hypothesize that an **RL**-based controller can also improve the robustness and reliability of the overall robot behavior.

As explained in Section V, one other key limitation was regarding the perception system. State estimation introduced a significant drift that caused a major noise and drift in the terrain map. Albeit not being a limitation to the suggested approach, we plan on improving the state estimation and perception system of **HyQ** and **HyQReal** to allow us to test **ViTAL** in the wild.

The pose optimization problem of the **VPA** does not reason about the robot's dynamics. This did not prevent **HyQ** and **HyQReal** from achieving dynamic locomotion while traversing challenging terrains at high speeds. However, we believe that incorporating the robot's dynamics into **ViTAL** may result in a better overall performance. That said, we believe that in the future, the **VPA** should also reason about the robot's dynamics. For instance, one can augment the **FEC** with another criterion that ensures that the selected footholds are dynamically feasible by the robot.

Additionally, in the future, we plan to extend the **VPA** of **ViTAL** to not only send pose references, but also reason about the robot's body twist. We also plan to augment the robot skills to not only consider foothold evaluation criteria, but also skills that are tailored to the robot pose. Finally, in this work, **ViTAL** considered heightmaps which are 2.5D maps. In the future, we plan to consider full 3D maps that will enable **ViTAL** to reason about navigating in confined space (inspired by [39]).

APPENDIX

A. CNN approximation in the VFA and the VPA

In the **VFA**, the foothold evaluation stage is approximated with a **CNN** [65] as explained in Remark 3. The **CNN** approximates the mapping between T_{vfa} and p_* . The heightmap H_{vfa} in T_{vfa} passes through three convolutional layers with 5×5 kernels, 2×2 padding, Leaky ReLU activation, and 2×2 max-pooling operation. The resulted one-dimensional feature vector is concatenated with the rest of the variables in the tuple T_{vfa} , namely, z_h , v_b , α , and p_n . This new vector passes through two fully-connected layers with Leaky ReLU and softmax activations. The parameters of the **CNN** are optimized to minimize the cross-entropy loss [67] of classifying a candidate foothold location as optimal p_* .

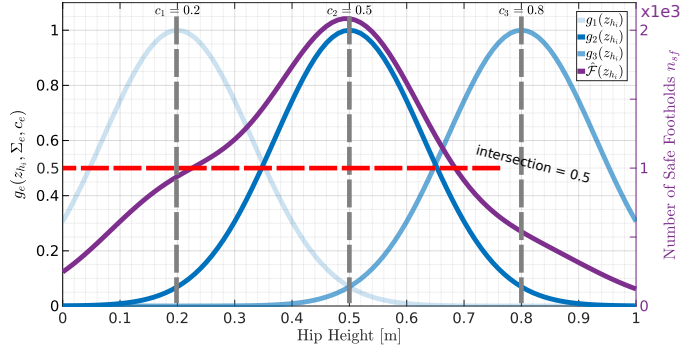


Fig. 15. An illustration of the Function Approximation of the **VPA**.

In the **VPA**, the pose evaluation and the function approximation is approximated with a **CNN** as explained in Remark 5. The **CNN** infers the weights w of $\hat{\mathcal{F}}$ given T_{vpa} (the mapping between T_{vpa} and w). The heightmap $H_{\text{vpa}} \in \mathbb{R}^{33 \times 33}$ passes through three convolutional layers with 5×5 kernels, 2×2 padding, Leaky ReLU activation, and 2×2 max-pooling operation. The body velocities v_b pass through a fully-connected layer with Leaky ReLU activation that is then concatenated with the one-dimensional feature vector obtained from the heightmap. This new vector passes through two fully-connected layers with Leaky ReLU and linear activations. The parameters of this **CNN** are optimized to minimize the mean squared error loss between the number of safe footholds n_{sf} predicted by $\hat{\mathcal{F}}(z_h, w)$ and $\hat{\mathcal{F}}(z_h, \hat{w})$ where \hat{w} are the function parameters approximated by the **CNN**.

For both **CNNs**, we used the Adam optimizer [68] with a learning rate of 0.001, and we used a validation-based early-stopping using a 9-to-1 proportion to reduce overfitting. The datasets required for training this **CNNs** are collected by running simulated terrain scenarios that consist of bars, gaps, stairs, and rocks. In this work, we considered a 33×33 heightmap with a resolution of 0.02 m ($H_{\text{vfa}}, H_{\text{vpa}} \in \mathbb{R}^{33 \times 33}$).

B. Details on the Function Approximation of the VPA

As explained in Section IV-D, the function $\hat{\mathcal{F}}(z_{hi}, w)$

$$\hat{\mathcal{F}}(z_{hi}, w) = \sum_{e=1}^E w_e \cdot g(z_{hi}, \Sigma_e, c_e) \quad (28)$$

is defined as the weighted sum of Gaussian basis functions

$$g(z_{hi}, \Sigma_e, c_e) = \exp(-0.5(z_{hi} - c_e)^T \Sigma_e^{-1} (z_{hi} - c_e)). \quad (29)$$

The parameters Σ_e and c_e are the widths and centers of the Gaussian function g_e (see Section 3.1 in [57]). In the literature, c_e is usually referred to as the mean or the expected value, and Σ_e as the standard deviation. The regression algorithm should predict the weights w_e , and the parameters Σ_e

and c_e . To reduce the dimensionality of the problem, as explained in Section IV-D, and in Section 4.1 in [57], we decided to fix the values of the parameters of the Gaussian functions Σ_e and c_e . In detail, the centers c_e are spaced equidistantly within the bounds of the hip heights z_{h_i} , and the widths are determined by the value at which the Gaussian functions intersect. That way, the regression algorithm only outputs the weights w_e . Figure 15 shows an example of the function approximation. In this example, the bounds of the hip heights z_{h_i} are 0.2 m and 0.8 m. Assuming a number of basis functions $E = 3$, the centers c_e are then chosen to be equidistant within the bounds, and thus, the centers c_e are 0.2 m, 0.3 m and 0.8 m. By choosing the Gaussian functions to intersect at 0.5, the widths Σ_e are 0.13.

C. Representing the Hip Heights in terms of the Body Pose

To represent the hip heights in terms of the body pose, we first write the forward kinematics of the robot's hips

$$p_{h_i}^W = p_b^W + R_b^W p_{h_i}^b \quad (30)$$

where $p_{h_i}^W \in \mathbb{R}^3$ is the position of the hip of the i th leg in the world frame, $p_b^W \in \mathbb{R}^3$ is the position of the robot's base in the world frame, $R_b^W \in SO(3)$ is the rotation matrix mapping vectors from the base frame to the world frame, and $p_{h_i}^b \in \mathbb{R}^3$ is the position of the hip of the i th leg in the base frame. The rotation matrix R_b^W is a representation of the Euler angles of the robot's base with sequence of roll β , pitch γ , and yaw ψ (Cardan angles) [69]. The variable $p_{h_i}^b$ is obtained from the CAD of the robot. Expanding (30) yields

$$\begin{bmatrix} x_{h_i}^W \\ y_{h_i}^W \\ z_{h_i}^W \end{bmatrix} = \begin{bmatrix} x_b^W \\ y_b^W \\ z_b^W \end{bmatrix} + R_b^W(\beta, \gamma, \psi) \begin{bmatrix} x_{h_i}^b \\ y_{h_i}^b \\ z_{h_i}^b \end{bmatrix} \quad (31)$$

$$= \begin{bmatrix} x_b^W \\ y_b^W \\ z_b^W \end{bmatrix} + \begin{bmatrix} \dots & \dots & \dots \\ \dots & \dots & \dots \\ -s\gamma & c\gamma & s\beta \\ c\gamma & c\gamma & c\beta \end{bmatrix} \begin{bmatrix} x_{h_i}^b \\ y_{h_i}^b \\ z_{h_i}^b \end{bmatrix} \quad (32)$$

where s and c are sine and cosine of the angles, respectively. Since we are interested only in the hip heights, the z-component (third row) of (32) yields

$$z_{h_i}^W = z_b^W - x_{h_i}^b s\gamma + y_{h_i}^b c\gamma s\beta + z_{h_i}^b c\gamma c\beta. \quad (33)$$

D. Details on Using the Sum of Squared Integrals as a Cost Function in the Pose Optimization Problem of the VPA

Using \mathcal{C}_{int} as a cost function can be motivated by taking Fig. 16 as an example. In this figure, there are two curves that represent $\hat{\mathcal{F}}_l$ where the horizontal axis is the hip height and the vertical axis represent n_{sf} . The figure shows two optimal poses where u_1^* is the optimal pose using the cost functions \mathcal{C}_{sum} or $\mathcal{C}_{\text{prod}}$ that only maximize for $\hat{\mathcal{F}}_l$, and u_2^* is the optimal pose using the cost function \mathcal{C}_{int} . As shown in the figure, if \mathcal{C}_{sum} or $\mathcal{C}_{\text{prod}}$ is used, the optimal pose will be u_1^* which is indeed the one that results in the maximum $\hat{\mathcal{F}}_l$. However, if there is a tracking error of m (thus the robot reaches $u_1^* \pm m$), the robot might end up in the pose $u_1^* \pm m$ that results in a small number of safe footholds. Using \mathcal{C}_{int} will take into account the safe footholds within a margin m .

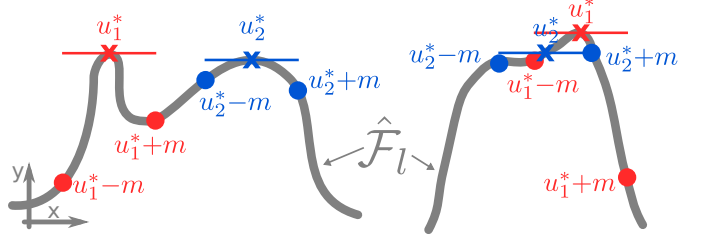


Fig. 16. Using the sum of squared integrals as a cost function in the pose optimization of the VPA. The two curves represent $\hat{\mathcal{F}}_l$. The x-axis is the hip height and the y-axis is n_{sf} . The figure shows two optimal poses: u_1^* which is from using \mathcal{C}_{sum} or $\mathcal{C}_{\text{prod}}$, and u_2^* which is from using \mathcal{C}_{int} .

This might result in a pose that does not yield the maximum number of safe footholds, but it will result in a safer foothold in case the robot pose has any tracking errors. Note that using the sum of squared integrals \mathcal{C}_{int} as a cost function is similar to smoothing $\hat{\mathcal{F}}_l$ with respect to the hip height (a moving average smoothing). Using a smoothing function \mathcal{C}_s may take the form

$$\mathcal{C}_s = \sum_{l=1}^{N_l=4} \left\| \frac{1}{2\epsilon} \sum_{i=-\epsilon}^{\epsilon} \hat{\mathcal{F}}_l(z_{h_l} + i) \right\|_Q^2. \quad (34)$$

E. Defining the Receding Horizon

In the receding horizon there is a tuple $T_{\text{vpa},j}$ for every j th horizon that is defined as

$$T_{\text{vpa},j} = (H_{\text{vpa},j}, v_b, \alpha) \quad (35)$$

hence sharing the same body twist v_b and gait parameters α but a different heightmap $H_{\text{vpa},j}$. For every leg, a heightmap of horizon $j+1$ is overlapping with the previous horizon's j heightmap. This overlap has a magnitude of Δh taking the same direction as the body velocity \dot{x}_b . Without loss of generality, we chose the magnitude of the overlap to be half of the diagonal size of the heightmap in this work. To sum up, we first gather $T_{\text{vpa},j}$ that share the same v_b and α , but a different $H_{\text{vpa},j}$. Then, we evaluate $T_{\text{vpa},j}$ and approximate the output using the function approximation yielding $\hat{\mathcal{F}}_j$ that is sent to the optimizer for all of the legs.

F. Miscellaneous Settings

In this work, all simulations were conducted on an Intel Core i7 quad-core CPU, and all experiments were running on an onboard Intel Core i7 quad-core CPU where state estimation, mapping, and controls were running. The RCF (including the WBC) runs at 250 Hz, the low-level controller runs at 1000 Hz, the state estimator runs at 333 Hz, and the mapping algorithm runs at 20 Hz. The VPA and the VFA run asynchronously at the maximum possible update rate.

ViTAL is implemented in Python. The CNNs are implemented in PyTorch [70]. As explained in Appendix A, in this work, we considered a 33×33 heightmap with a resolution of 0.02 m ($H_{\text{vfa}}, H_{\text{vpa}} \in \mathbb{R}^{33 \times 33}$). The finite set $\bar{\mathcal{Z}}$ consisted of a hip height range between 0.2 m and 0.8 m with a resolution of 0.02 m yielding $N_{z_h} = 31$ samples. The number of radial basis functions used in the function

approximation was $E = 30$. The pose optimization problem is solved with a trust-region interior point method [71], [72] which is a non-linear optimization problem solver that we solved using SciPy [73]. The bounds of the pose optimization problem u_{\min} and u_{\max} are $[0.2 \text{ m}, -0.35 \text{ rad}, -0.35 \text{ rad}]$, and $[0.8 \text{ m}, 0.35 \text{ rad}, 0.35 \text{ rad}]$, respectively. We used a receding horizon of $N_h = 2$ with a map overlap of half the size of the heightmap. For a heightmap of a size of 33×33 and a resolution of 0.02 m, the map overlap Δh is 0.33 m. We used Gazebo [74] for the simulations, and ROS for communication.

G. Estimation Accuracy

We compare the estimation accuracy of the **VFA** by comparing the output of the foothold evaluation stage (explained in Section III) given the same input tuple T_{vfa} . That is to say, we compare the estimation accuracy of the **VFA** by comparing $\hat{g}(T_{\text{vfa}})$ versus $g(T_{\text{vfa}})$ (see Remark 3). To do so, once trained, we generated a dataset of 4401 samples from randomly sampled heightmaps for every leg. This analysis was done on **HyQ**.

As explained in Section III, from all of the safe candidate footholds in μ_{safe} , the **VFA** chooses the optimal foothold to be the one closest to the nominal foothold. Thus, to fairly analyse the estimation accuracy of the **VFA**, we present three main measures: *perfect match* being the amount of samples where $\hat{g}(T_{\text{vfa}})$ outputted the exact value of $g(T_{\text{vfa}})$, *safe footholds*, being the amount of samples where $\hat{g}(T_{\text{vfa}})$ did not output the exact value of $g(T_{\text{vfa}})$, but rather a foothold that is safe but not closest to the nominal foothold, and *mean distance*, being the average distance of the estimated optimal foothold from $\hat{g}(T_{\text{vfa}})$ relative to the exact foothold from $g(T_{\text{vfa}})$. These measures are presented as the mean of all legs.

Based on that, the perfect match measure is 74.0%. Thus, 74% of $\hat{g}(T_{\text{vfa}})$ perfectly matched $g(T_{\text{vfa}})$. The safe footholds measure is 93.7%. Thus, 93.7% of $\hat{g}(T_{\text{vfa}})$ were deemed safe. Finally, the mean distance of the estimated optimal foothold from $\hat{g}(T_{\text{vfa}})$ relative to the exact foothold from $g(T_{\text{vfa}})$ is 0.02 m. This means that, on average, $\hat{g}(T_{\text{vfa}})$ yielded optimal footholds that are 0.02 m far from the optimal foothold from $g(T_{\text{vfa}})$. Note that, the radius of **HyQ**'s foot, and the resolution of the heightmap is also 0.02 m, which means that the average distance measure is still acceptable especially since we account for this value in the uncertainty margin as explained in Remark 1.

Similar to the **VFA**, we compare the accuracy of **VPA** by comparing the output of the pose evaluation stage (explained in Section IV-C) given the same input tuple T_{vfa} . That is to say, we compare the estimation accuracy of the **VPA** by comparing $\bar{\mathcal{F}}$ versus $\hat{\mathcal{F}}$ (see Remark 4 and Remark 5). To do so, we ran one simulation using the stairs setup shown in Fig. 5 on **HyQ**, and gathered the input tuple T_{vfa} . Then, we ran the **VPA** offline, once with the exact evaluation (yielding $\bar{\mathcal{F}}$) and once with the approximate one (yielding $\hat{\mathcal{F}}$).

Based on this simulation run, the mean values of the exact and the approximate evaluations are $\text{mean}(\bar{\mathcal{F}}) = 1370$ and $\text{mean}(\hat{\mathcal{F}}) = 1322$, respectively. This yields an estimation accuracy $\text{mean}(\hat{\mathcal{F}})/\text{mean}(\bar{\mathcal{F}})$ of 96.5%.

H. Computational Analysis

To analyze the computational time of the **VFA** and the **VPA**, we ran one simulation using the stairs setup shown in Fig. 5 on **HyQ** to gather the input tuples of the **VFA** and the **VPA**, T_{vfa} and T_{vpa} , respectively. Then, we ran both algorithms offline, once with the exact evaluation and once using the **CNNs**, and collected the time it took to run both algorithms (all stages included). The mean and standard deviation of the time taken to compute the exact and the **CNN**-approximated **VFA** (per leg) algorithms are $7.5 \text{ ms} \pm 1 \text{ ms}$, and $3.5 \text{ ms} \pm 1 \text{ ms}$, respectively. The mean and standard deviation of the time taken to compute the exact and the **CNN**-approximated **VPA** algorithms are $720 \text{ ms} \pm 68 \text{ ms}$, and $180 \text{ ms} \pm 60 \text{ ms}$, respectively. Hence, the **VFA** and the **VPA** can run at roughly 280 Hz and 5 Hz, respectively. This also shows that the **CNNs** can speed up the evaluation of the **VFA** and the **VPA** up to 4 times and 2 times, respectively.

Note that it takes longer to compute the **VFA** of this work versus our previous work [38]. This is because the **VFA** of this work considers more inputs than in our previous work, and thus, the size of the **CNN** is larger. As can be seen, the **VPA** runs at a relatively lower update rate compared to the **VFA**. We believe that this is not an issue since the **VFA** runs at the legs-level while the **VPA** runs as the body-level which means that the legs experience faster dynamics than the body.

During simulations and experiments, the **CNNs** were running on a CPU. A significant amount of computational time can be reduced if we run the **CNNs** of the **VFA** and the **VPA** on a GPU. Likewise, a significant amount of computational time can be reduced if a different pose optimization solver is used. However, both suggestions are beyond the scope of this work, and are left as a future work.

I. Abbreviations

F	Set of Safe Footholds
n_{sf}	Number of Safe Footholds
CNN	Convolutional Neural Network
FC	Foot Trajectory Collision
FEC	Foothold Evaluation Criteria
HyQ	Hydraulically actuated Quadruped
KF	Kinematic Feasibility
LC	Leg Collision
MPC	Model Predictive Control
RCF	Reactive Controller Framework
RL	Reinforcement Learning
TAL	Terrain-Aware Locomotion
TBR	Terrain-Based Body Reference
TO	Trajectory Optimization
TR	Terrain Roughness
VFA	Vision-Based Foothold Adaptation
ViTAL	Vision-Based Terrain-Aware Locomotion
VPA	Vision-Based Pose Adaptation
WBC	Whole-Body Controller

ACKNOWLEDGMENTS

The authors would like to thank Geoff Fink and Chundri Boelens for the help provided in this work.

REFERENCES

- [1] J. Lee, J. Hwangbo, L. Wellhausen, V. Koltun, and M. Hutter, "Learning quadrupedal locomotion over challenging terrain," *Sci. Robot.*, vol. 5, no. 47, p. eabc5986, Oct. 2021, DOI:[10.1126/scirobotics.abc5986](https://doi.org/10.1126/scirobotics.abc5986).
- [2] C. Yang, K. Yuan, Q. Zhu, W. Yu, and Z. Li, "Multi-expert learning of adaptive legged locomotion," *Sci. Robot.*, vol. 5, no. 49, p. eabb2174, Dec. 2020, DOI:[10.1126/scirobotics.abb2174](https://doi.org/10.1126/scirobotics.abb2174).
- [3] C. Semini, V. Barasuol, M. Focchi, C. Boelens, M. Emara, S. Casella, O. Villarreal, R. Orsolino, G. Fink, S. Fahmi, G. Medrano-Cerda, and D. G. Caldwell, "Brief introduction to the quadruped robot HyQReal," in *Italian Conference on Robotics and Intelligent Machines (I-RIM)*, Rome, Italy, Oct. 2019, pp. 1–2.
- [4] B. Katz, J. D. Carlo, and S. Kim, "Mini cheetah: A platform for pushing the limits of dynamic quadruped control," in *Proc. IEEE Int. Conf. Robot. Automat. (ICRA)*, Montreal, QC, Canada, May 2019, pp. 6295–6301, DOI:[10.1109/ICRA.2019.8793865](https://doi.org/10.1109/ICRA.2019.8793865).
- [5] G. Bledt, M. J. Powell, B. Katz, J. Di Carlo, P. M. Wensing, and S. Kim, "MIT Cheetah 3: Design and control of a robust, dynamic quadruped robot," in *Proc. IEEE/RSJ Int. Conf. Intell. Robot. Syst. (IROS)*, Madrid, Spain, Oct. 2018, pp. 2245–2252, DOI:[10.1109/IROS.2018.8593885](https://doi.org/10.1109/IROS.2018.8593885).
- [6] M. Hutter, C. Gehring, D. Jud, A. Lauber, C. D. Bellicoso, V. Tsounis, J. Hwangbo, K. Bodie, P. Fankhauser, M. Bloesch, R. Diethelm, S. Bachmann, A. Melzer, and M. Hoepflinger, "Anymal - a highly mobile and dynamic quadrupedal robot," in *Proc. IEEE/RSJ Int. Conf. Intell. Robot. Syst. (IROS)*, Daejeon, South Korea, Oct. 2016, pp. 38–44, DOI:[10.1109/IROS.2016.7758092](https://doi.org/10.1109/IROS.2016.7758092).
- [7] Boston Dynamics, Spot, 2021, <https://www.bostondynamics.com/spot>, [Online; accessed Aug. 2022].
- [8] Agility Robotics, Robots, 2021, <https://www.agilityrobotics.com/robots>, [Online; accessed Aug. 2022].
- [9] Unitree Robotics, Go1, 2021, <https://www.unitree.com/products/go1>, [Online; accessed Aug. 2022].
- [10] S. Fahmi, "On terrain-aware locomotion for legged robots," Ph.D. dissertation, Istituto Italiano di Tecnologia (IIT), Apr. 2021. [Online]. Available: <https://arxiv.org/abs/2212.00683>
- [11] R. Buchanan, J. Bednarek, M. Camurri, M. Nowicki, K. Walas, and M. Fallon, "Navigating by touch: haptic monte carlo localization via geometric sensing and terrain classification," *Auton. Robot.*, vol. 45, pp. 843–857, Aug. 2021, DOI:<https://doi.org/10.1007/s10514-021-10013-w>.
- [12] S. Fahmi, G. Fink, and C. Semini, "On state estimation for legged locomotion over soft terrain," *IEEE Sens. Lett. (L-SENS)*, vol. 5, no. 1, pp. 1–4, Jan. 2021.
- [13] S. Wang, A. Bhatia, M. T. Mason, and A. M. Johnson, "Contact localization using velocity constraints," in *Proc. IEEE/RSJ Int. Conf. Intell. Robot. Syst. (IROS)*, Las Vegas, NV, USA (Virtual), Oct. 2020, pp. 7351–7358.
- [14] A. Ahmadi, T. Nygaard, N. Kottege, D. Howard, and N. Hudson, "Semi-supervised gated recurrent neural networks for robotic terrain classification," *IEEE Robot. Automat. Lett. (RA-L)*, vol. 6, no. 2, pp. 1848–1855, Feb. 2021, DOI:[10.1109/LRA.2021.3060437](https://doi.org/10.1109/LRA.2021.3060437).
- [15] H. C. Lin and M. Mistry, "Contact surface estimation via haptic perception," in *Proc. IEEE Int. Conf. Robot. Automat. (ICRA)*, Paris, France (Virtual), May 2020, pp. 5087–5093, DOI:[10.1109/ICRA40945.2020.9196816](https://doi.org/10.1109/ICRA40945.2020.9196816).
- [16] S. Fahmi, M. Focchi, A. Radulescu, G. Fink, V. Barasuol, and C. Semini, "Stance: Locomotion adaptation over soft terrain," *IEEE Trans. Robot. (T-RO)*, vol. 36, no. 2, pp. 443–457, Apr. 2020, DOI:[10.1109/TRO.2019.2954670](https://doi.org/10.1109/TRO.2019.2954670).
- [17] K. Paigwar, L. Krishna, S. Tirumala, N. Khetan, A. Sagi, A. Joglekar, S. Bhatnagar, A. Ghosal, B. Amrutur, and S. Kolathaya, "Robust quadrupedal locomotion on sloped terrains: A linear policy approach," in *Proc. Conf. Robot Learn. (CoRL)*, Virtual, Nov. 2020, pp. 1–11.
- [18] L. Wellhausen, A. Dosovitskiy, R. Ranftl, K. Walas, C. Cadena, and M. Hutter, "Where should i walk? predicting terrain properties from images via self-supervised learning," *IEEE Robot. Automat. Lett. (RA-L)*, vol. 4, no. 2, pp. 1509–1516, Jan. 2019, DOI:[10.1109/LRA.2019.2895390](https://doi.org/10.1109/LRA.2019.2895390).
- [19] W. Bosworth, J. Whitney, Sangbae Kim, and N. Hogan, "Robot locomotion on hard and soft ground: Measuring stability and ground properties in-situ," in *Proc. IEEE Int. Conf. Robot. Automat. (ICRA)*, Stockholm, Sweden, May 2016, pp. 3582–3589, DOI:[10.1109/ICRA.2016.7487541](https://doi.org/10.1109/ICRA.2016.7487541).
- [20] D. D. Fan, K. Otsu, Y. Kubo, A. Dixit, J. Burdick, and A. Aghamohammadi, "STEP: Stochastic Traversability Evaluation and Planning for Risk-Aware Off-road Navigation," in *Proc. Robot.: Sci. and Syst. (RSS)*, Virtual, Jul. 2021, pp. 1–12, DOI:[10.15607/RSS.2021.XVII.021](https://doi.org/10.15607/RSS.2021.XVII.021).
- [21] O. Melon, R. Orsolino, D. Surovik, M. Geisert, I. Havoutis, and M. Fallon, "Receding-horizon perceptive trajectory optimization for dynamic legged locomotion with learned initialization," in *Proc. IEEE Int. Conf. Robot. Automat. (ICRA)*, Xi'an, China (Virtual), Jun. 2021, pp. 9805–9811, DOI:[10.1109/ICRA48506.2021.9560794](https://doi.org/10.1109/ICRA48506.2021.9560794).
- [22] B. Ponton, M. Khadiv, A. Meduri, and L. Righetti, "Efficient multi-contact pattern generation with sequential convex approximations of the centroidal dynamics," *IEEE Trans. Robot. (T-RO)*, vol. 37, no. 5, pp. 1661–1679, Feb. 2021, DOI:[10.1109/TRO.2020.3048125](https://doi.org/10.1109/TRO.2020.3048125).
- [23] C. Mastalli, R. Budhiraja, W. Merkt, G. Saurel, B. Hammoud, M. Naveau, J. Carpentier, L. Righetti, S. Vijayakumar, and N. Mansard, "CrocoddyL: An efficient and versatile framework for multi-contact optimal control," in *Proc. IEEE Int. Conf. Robot. Automat. (ICRA)*, Virtual, May 2020, pp. 2536–2542, DOI:[10.1109/ICRA40945.2020.9196673](https://doi.org/10.1109/ICRA40945.2020.9196673).
- [24] A. W. Winkler, C. D. Bellicoso, M. Hutter, and J. Buchli, "Gait and trajectory optimization for legged systems through phase-based end-effector parameterization," *IEEE Robot. Automat. Lett. (RA-L)*, vol. 3, no. 3, pp. 1560–1567, Feb. 2018, DOI:[10.1109/LRA.2018.2798285](https://doi.org/10.1109/LRA.2018.2798285).
- [25] C. Mastalli, I. Havoutis, M. Focchi, D. G. Caldwell, and C. Semini, "Motion planning for quadrupedal locomotion: Coupled planning, terrain mapping and whole-body control," *IEEE Trans. Robot. (T-RO)*, vol. 36, no. 6, pp. 1635–1648, Apr. 2020, DOI:[10.1109/TRO.2020.3003464](https://doi.org/10.1109/TRO.2020.3003464).
- [26] M. Brunner, B. Brüggemann, and D. Schulz, "Hierarchical rough terrain motion planning using an optimal sampling-based method," in *Proc. IEEE Int. Conf. Robot. Automat. (ICRA)*, Karlsruhe, Germany, May 2013, pp. 5539–5544, DOI:[10.1109/ICRA.2013.6631372](https://doi.org/10.1109/ICRA.2013.6631372).
- [27] H. Li and P. M. Wensing, "Hybrid systems differential dynamic programming for whole-body motion planning of legged robots," *IEEE Robot. Automat. Lett. (RA-L)*, vol. 5, no. 4, pp. 5448–5455, Jul. 2020, DOI:[10.1109/LRA.2020.3007475](https://doi.org/10.1109/LRA.2020.3007475).
- [28] H. Li, R. J. Frei, and P. M. Wensing, "Model hierarchy predictive control of robotic systems," *IEEE Robot. Automat. Lett. (RA-L)*, vol. 6, no. 2, pp. 3373–3380, Feb. 2021, DOI:[10.1109/LRA.2021.3061322](https://doi.org/10.1109/LRA.2021.3061322).
- [29] N. Rudin, D. Hoeller, P. Reist, and M. Hutter, "Learning to walk in minutes using massively parallel deep reinforcement learning," in *Proc. Conf. Robot Learn. (CoRL)*, London, UK, Nov. 2021, pp. 91–100.
- [30] W. Yu, D. Jain, A. Escontrela, A. Iscen, , P. Xu, E. Coumans, S. Ha, J. Tan, and T. Zhang, "Visual-locomotion: Learning to walk on complex terrains with vision," in *Proc. Conf. Robot Learn. (CoRL)*, London, UK, Nov. 2021, pp. 1291–1302.
- [31] T. Miki, J. Lee, J. Hwangbo, L. Wellhausen, V. Koltun, and M. Hutter, "Learning robust perceptive locomotion for quadrupedal robots in the wild," *Sci. Robot.*, vol. 7, no. 62, p. eabk2822, Jan. 2022, DOI:[10.1126/scirobotics.abk2822](https://doi.org/10.1126/scirobotics.abk2822).
- [32] S. Gangapurwala, M. Geisert, R. Orsolino, M. Fallon, and I. Havoutis, "Real-time trajectory adaptation for quadrupedal locomotion using deep reinforcement learning," in *Proc. IEEE Int. Conf. Robot. Automat. (ICRA)*, Xi'an, China (Virtual), Oct. 2021, pp. 1–7.
- [33] A. Kumar, Z. Fu, D. Pathak, and J. Malik, "RMA: Rapid motor adaptation for legged robots," in *Proc. Robot.: Sci. and Syst. (RSS)*, Virtual, Jul. 2021, pp. 1–15, DOI:[10.15607/RSS.2021.XVII.011Fe](https://doi.org/10.15607/RSS.2021.XVII.011Fe).
- [34] J. Siekmann, K. Green, J. Warila, A. Fern, and J. Hurst, "Blind bipedal stair traversal via sim-to-real reinforcement learning," in *Proc. Robot.: Sci. and Syst. (RSS)*, Virtual, Jul. 2021, pp. 1–9, DOI:[10.15607/RSS.2021.XVII.061](https://doi.org/10.15607/RSS.2021.XVII.061).
- [35] V. Tsounis, M. Alge, J. Lee, F. Farshidian, and M. Hutter, "Deepgait: Planning and control of quadrupedal gaits using deep reinforcement learning," *IEEE Robot. Automat. Lett. (RA-L)*, vol. 5, no. 2, pp. 3699–3706, Mar. 2020, DOI:[10.1109/LRA.2020.2979660](https://doi.org/10.1109/LRA.2020.2979660).
- [36] M. Kalakrishnan, J. Buchli, P. Pastor, M. Mistry, and S. Schaal, "Learning, planning, and control for quadruped locomotion over challenging terrain," *Int. J. Robot. Res. (IJRR)*, vol. 30, no. 2, pp. 236–258, Nov. 2011, DOI:[10.1177/0278364910388677](https://doi.org/10.1177/0278364910388677).
- [37] P. Fankhauser, M. Bjelonic, C. Dario Bellicoso, T. Miki, and M. Hutter, "Robust rough-terrain locomotion with a quadrupedal robot," in *Proc. IEEE Int. Conf. Robot. Automat. (ICRA)*, Brisbane, QLD, Australia, May 2018, pp. 5761–5768, DOI:[10.1109/ICRA.2018.8460731](https://doi.org/10.1109/ICRA.2018.8460731).
- [38] O. Villarreal, V. Barasuol, M. Camurri, L. Franceschi, M. Focchi, M. Pontil, D. G. Caldwell, and C. Semini, "Fast and continuous foothold adaptation for dynamic locomotion through cnns," *IEEE Robot. Automat. Lett. (RA-L)*, vol. 4, no. 2, pp. 2140–2147, Feb. 2019, DOI:[10.1109/LRA.2019.2899434](https://doi.org/10.1109/LRA.2019.2899434).
- [39] R. Buchanan, L. Wellhausen, M. Bjelonic, T. Bandyopadhyay, N. Kottege, and M. Hutter, "Perceptive whole-body planning for multilegged robots in confined spaces," *J. Field Robot.*, vol. 38, no. 1, pp. 68–84, Jun. 2021, DOI:[10.1002/rob.21974](https://doi.org/10.1002/rob.21974).

- [40] P. Fernbach, S. Tonneau, and M. Taix, "CROC: Convex resolution of centroidal dynamics trajectories to provide a feasibility criterion for the multi contact planning problem," in *Proc. IEEE/RSJ Int. Conf. Intell. Robot. Syst. (IROS)*, Madrid, Spain, Oct. 2018, pp. 8367–8373, DOI:[10.1109/IROS.2018.8593888](https://doi.org/10.1109/IROS.2018.8593888).
- [41] S. Tonneau, A. Del Prete, J. Pettré, C. Park, D. Manocha, and N. Mansard, "An efficient acyclic contact planner for multiped robots," *IEEE Trans. Robot. (T-RO)*, vol. 34, no. 3, pp. 586–601, Apr. 2018, DOI:[10.1109/TRO.2018.2819658](https://doi.org/10.1109/TRO.2018.2819658).
- [42] J. Z. Kolter, M. P. Rodgers, and A. Y. Ng, "A control architecture for quadruped locomotion over rough terrain," in *Proc. IEEE Int. Conf. Robot. Automat. (ICRA)*, Pasadena, CA, USA, May 2008, pp. 811–818, DOI:[10.1109/ROBOT.2008.4543305](https://doi.org/10.1109/ROBOT.2008.4543305).
- [43] M. Kalakrishnan, J. Buchli, P. Pastor, and S. Schaal, "Learning locomotion over rough terrain using terrain templates," in *Proc. IEEE/RSJ Int. Conf. Intell. Robot. Syst. (IROS)*, St. Louis, MO, USA, Oct. 2009, pp. 167–172, DOI:[10.1109/IROS.2009.5354701](https://doi.org/10.1109/IROS.2009.5354701).
- [44] D. Belter and S. Piotr, "Rough terrain mapping and classification for foothold selection in a walking robot," *J. Field Robot.*, vol. 28, no. 4, pp. 497–528, Jun. 2011, DOI:[10.1002/rob.20397](https://doi.org/10.1002/rob.20397).
- [45] V. Barasuol, M. Camurri, S. Bazeille, D. G. Caldwell, and C. Semini, "Reactive trotting with foot placement corrections through visual pattern classification," in *Proc. IEEE/RSJ Int. Conf. Intell. Robot. Syst. (IROS)*, Hamburg, Germany, Sep. 2015, pp. 5734–5741, DOI:[10.1109/IROS.2015.7354191](https://doi.org/10.1109/IROS.2015.7354191).
- [46] F. Jenelten, T. Miki, A. E. Vijayan, M. Bjelonic, and M. Hutter, "Perceptive locomotion in rough terrain – online foothold optimization," *IEEE Robot. Automat. Lett. (RA-L)*, vol. 5, no. 4, pp. 5370–5376, Jul. 2020, DOI:[10.1109/LRA.2020.3007427](https://doi.org/10.1109/LRA.2020.3007427).
- [47] D. Song, P. Fernbach, T. Flayols, A. Del Prete, N. Mansard, S. Tonneau, and Y. J. Kim, "Solving footprint planning as a feasibility problem using 11-norm minimization," *IEEE Robot. Automat. Lett. (RA-L)*, vol. 6, no. 3, pp. 5961–5968, Jun. 2021, DOI:[10.1109/LRA.2021.3088797](https://doi.org/10.1109/LRA.2021.3088797).
- [48] D. Belter, J. Bednarek, H. Lin, G. Xin, and M. Mistry, "Single-shot foothold selection and constraint evaluation for quadruped locomotion," in *Proc. IEEE Int. Conf. Robot. Automat. (ICRA)*, Montreal, QC, Canada, May 2019, pp. 7441–7447, DOI:[10.1109/ICRA.2019.8793801](https://doi.org/10.1109/ICRA.2019.8793801).
- [49] D. Esteban, O. Villarreal, S. Fahmi, C. Semini, and V. Barasuol, "On the influence of body velocity in foothold adaptation for dynamic legged locomotion via cnns," in *Proc. Int. Conf. Clim. Walk. Robot. (CLAWAR)*, Moscow, Russia, Aug. 2020, pp. 353–360, DOI:[10.13180/clawar.2020.24-26.08.62](https://doi.org/10.13180/clawar.2020.24-26.08.62).
- [50] D. Kim, D. Carballo, J. Di Carlo, B. Katz, G. Bledt, B. Lim, and S. Kim, "Vision aided dynamic exploration of unstructured terrain with a small-scale quadruped robot," in *Proc. IEEE Int. Conf. Robot. Automat. (ICRA)*, Paris, France (Virtual), May 2020, pp. 2464–2470, DOI:[10.1109/ICRA40945.2020.9196777](https://doi.org/10.1109/ICRA40945.2020.9196777).
- [51] D. Belter and S. Piotr, "Posture optimization strategy for a statically stable robot traversing rough terrain," in *Proc. IEEE/RSJ Int. Conf. Intell. Robot. Syst. (IROS)*, Vilamoura, Portugal, Oct. 2012, pp. 2204–2209, DOI:[10.1109/IROS.2012.6385548](https://doi.org/10.1109/IROS.2012.6385548).
- [52] D. Belter, "Efficient modeling and evaluation of constraints in path planning for multi-legged walking robots," *IEEE Access*, vol. 7, pp. 107 845–107 862, Aug. 2019, DOI:[10.1109/ACCESS.2019.2933178](https://doi.org/10.1109/ACCESS.2019.2933178).
- [53] O. Villarreal, V. Barasuol, P. M. Wensing, D. G. Caldwell, and C. Semini, "Mpc-based controller with terrain insight for dynamic legged locomotion," in *Proc. IEEE Int. Conf. Robot. Automat. (ICRA)*, Paris, France (Virtual), May 2020, pp. 2436–2442, DOI:[10.1109/ICRA40945.2020.9197312](https://doi.org/10.1109/ICRA40945.2020.9197312).
- [54] R. Buchanan, M. Camurri, and M. Fallon, "Haptic sequential monte carlo localization for quadrupedal locomotion in vision-denied scenarios," in *Proc. IEEE/RSJ Int. Conf. Intell. Robot. Syst. (IROS)*, Las Vegas, NV, USA (Virtual), Oct. 2020, pp. 3657–3663.
- [55] K. Green, Y. Godse, J. Dao, R. L. Hatton, A. Fern, and J. Hurst, "Learning spring mass locomotion: Guiding policies with a reduced-order model," *IEEE Robot. Automat. Lett. (RA-L)*, vol. 6, no. 2, pp. 3926–3932, Mar. 2021, DOI:[10.1109/LRA.2021.3066833](https://doi.org/10.1109/LRA.2021.3066833).
- [56] V. Barasuol, J. Buchli, C. Semini, M. Frigerio, E. R. De Pieri, and D. G. Caldwell, "A reactive controller framework for quadrupedal locomotion on challenging terrain," in *Proc. IEEE Int. Conf. Robot. Automat. (ICRA)*, Karlsruhe, Germany, May 2013, pp. 2554–2561, DOI:[10.1109/ICRA.2013.6630926](https://doi.org/10.1109/ICRA.2013.6630926).
- [57] F. Stulp and O. Sigaud, "Many regression algorithms, one unified model: A review," *Neural Networks*, vol. 69, pp. 60–79, Sep. 2015, DOI:[10.1016/j.neunet.2015.05.005](https://doi.org/10.1016/j.neunet.2015.05.005).
- [58] M. Focchi, V. Barasuol, I. Havoutis, J. Buchli, C. Semini, and D. Gladwell, "Local reflex generation for obstacle negotiation in quadrupedal locomotion," in *Proc. Int. Conf. Clim. Walk. Robot. (CLAWAR)*, Sydney, Australia, Jul. 2013, pp. 443–450, DOI:[10.1142/9789814525534_0056](https://doi.org/10.1142/9789814525534_0056).
- [59] S. Fahmi, C. Mastalli, M. Focchi, and C. Semini, "Passive whole-body control for quadruped robots: Experimental validation over challenging terrain," *IEEE Robot. Automat. Lett. (RA-L)*, vol. 4, no. 3, pp. 2553–2560, Jul. 2019, DOI:[10.1109/LRA.2019.2908502](https://doi.org/10.1109/LRA.2019.2908502).
- [60] T. Boaventura, J. Buchli, C. Semini, and D. Caldwell, "Model-based hydraulic impedance control for dynamic robots," *IEEE Trans. Robot. (T-RO)*, vol. 31, no. 6, pp. 1324–1336, Dec. 2015, DOI:[10.1109/TRO.2015.2482061](https://doi.org/10.1109/TRO.2015.2482061).
- [61] M. Camurri, M. Fallon, S. Bazeille, A. Radulescu, V. Barasuol, D. G. Caldwell, and C. Semini, "Probabilistic contact estimation and impact detection for state estimation of quadruped robots," *IEEE Robot. Automat. Lett. (RA-L)*, vol. 2, no. 2, pp. 1023–1030, Apr. 2017, DOI:[10.1109/LRA.2017.2652491](https://doi.org/10.1109/LRA.2017.2652491).
- [62] C. Semini, N. G. Tsagarakis, E. Guglielmino, M. Focchi, F. Cannella, and D. G. Caldwell, "Design of HyQ – a hydraulically and electrically actuated quadruped robot," *Proc. Inst. Mech. Eng. Part I J. Syst. Control Eng.*, vol. 225, no. 6, pp. 831–849, 2011, DOI:[10.1177/095651811402275](https://doi.org/10.1177/095651811402275).
- [63] P. Fankhauser and M. Hutter, "A universal grid map library: Implementation and use case for rough terrain navigation," in *Robot Operating System (ROS): The Complete Reference*, A. Koubaa, Ed. Cham, Switzerland: Springer International Publishing, Feb. 2016, vol. 1, pp. 99–120, DOI:[10.1007/978-3-319-26054-9_5](https://doi.org/10.1007/978-3-319-26054-9_5).
- [64] S. Fahmi, V. Barasuol, D. Esteban, O. Villarreal, and C. Semini, "ViTAL Accompanying Video," Youtube, Nov. 2021, <https://youtu.be/b5Ea7Jf6hbo>. [Online; accessed Aug. 2022].
- [65] Y. Le Cun, B. Boser, J. S. Denker, D. Henderson, R. E. Howard, and L. D. J. W. Hubbard, "Handwritten digit recognition with a back-propagation network," in *Proc. Int. Conf. Neural Inf. Process. Syst. (NeurIPS)*, Cambridge, MA, USA, Jan. 1989, pp. 396–404.
- [66] A. L. Maas, A. Y. Hannun, and A. Y. Ng, "Rectifier nonlinearities improve neural network acoustic models," in *Proc. Int. Conf. Mach. Learn. (ICML)*, Atlanta, GA, USA, Jun. 2013, pp. 1–6.
- [67] C. M. Bishop, *Pattern Recognition and Machine Learning*, 1st ed. New York, NY, USA: Springer-Verlag, 2006.
- [68] D. P. Kingma and J. L. Ba, "Adam: A method for stochastic optimization," in *Proc. Int. Conf. Learn. Repr. (ICLR)*, San Diego, CA, USA, May 2015, pp. 1–15. [Online]. Available: <http://arxiv.org/abs/1412.6980>
- [69] J. Diebel, "Representing attitude: Euler angles, unit quaternions, and rotation vectors," Stanford University, Stanford, CA, US, Tech. Rep., Oct. 2006.
- [70] A. Paszke, S. Gross, F. Massa, A. Lerer, J. Bradbury, G. Chanan, T. Killeen, Z. Lin, N. Gimelshein, L. Antiga, A. Desmaison, A. Kopf, E. Yang, Z. DeVito, M. Raison, A. TEjani, S. Chilamkurthy, B. Steiner, L. Fang, J. Bai, and S. Chintala, "PyTorch: An imperative style, high-performance deep learning library," in *Proc. Int. Conf. Neural Inf. Process. Syst. (NeurIPS)*, Vancouver, Canada, Dec. 2019, pp. 8026–8037.
- [71] J. Nocedal and S. J. Wright, *Numerical Optimization*, 1996, vol. 17, DOI:[10.1097/0003446-199604000-00005](https://doi.org/10.1097/0003446-199604000-00005).
- [72] R. H. Byrd, M. E. Hribar, and J. Nocedal, "An interior point algorithm for large-scale nonlinear programming," *SIAM Journal on Optimization*, vol. 9, no. 4, pp. 877–900, Sep. 2021, DOI:[10.1137/S1052623497325107](https://doi.org/10.1137/S1052623497325107).
- [73] P. Virtanen, R. Gommers, T. E. Oliphant, M. Haberland, T. Reddy, D. Cournapeau, E. Burovski, P. Peterson, W. Weckesser, J. Bright, S. J. van der Walt, M. Brett, J. Wilson, K. J. Millman, N. Mayorov, A. R. J. Nelson, E. Jones, R. Kern, E. Larson, C. J. Carey, I. Polat, Y. Feng, E. W. Moore, J. VanderPlas, D. Laxalde, J. Perktold, R. Cimrman, I. Henriksen, E. A. Quintero, C. R. Harris, A. M. Archibald, A. H. Ribeiro, F. Pedregosa, P. van Mulbregt, and SciPy 1.0 Contributors, "SciPy 1.0: Fundamental algorithms for scientific computing in python," *Nature Methods*, vol. 17, no. 3, pp. 261–272.
- [74] N. Koenig and A. Howard, "Design and use paradigms for gazebo, an open-source multi-robot simulator," in *Proc. IEEE/RSJ Int. Conf. Intell. Robot. Syst. (IROS)*, St. Louis, MO, USA, Oct. 2004, pp. 2149–2154, DOI:[10.1109/IROS.2004.1389727](https://doi.org/10.1109/IROS.2004.1389727).



Shamel Fahmi (S'19) was born in Cairo, Egypt. He received the B.Sc. degree in Mechatronics from the German University in Cairo, Cairo, Egypt, in 2015, the M.Sc. degree in Systems and Control from the University of Twente, Enschede, the Netherlands, in 2017, and the Ph.D. degree in Advanced and Humanoid Robotics from the Italian Institute of Technology, Genoa, Italy, in 2021. His Ph.D. was on terrain-aware locomotion for legged robots. Currently, he is researcher at the Biomimetic Robotics Lab, Massachusetts Institute of Technology, MA, USA. His research interests include locomotion planning and control for quadruped and humanoid robots using model- and learning-based methods.



Claudio Semini (S'07-M'10) received the M.Sc. degree in electrical engineering and information technology from ETH, Zurich, Switzerland, in 2005, and the Ph.D. degree in humanoid technologies from Istituto Italiano di Tecnologia (IIT), Genoa, Italy, in 2010. During his doctorate, he developed the hydraulic quadruped robot HyQ and worked on its control. Since 2012, he leads the Dynamic Legged Systems (DLS) lab. He is a co-founder of the Technical Committee on Mechanisms and Design of the IEEE-RAS Society. He is/was the coordinator/partner of several EU-, National and Industrial projects (including HyQ-REAL, INAIL Teleop, Moog@IIT joint lab, ESA-ANT, etc). His research interests include the design and control of highly dynamic and versatile legged robots for real-world operations, locomotion, hydraulics, and others.



Victor Barasuol received the Diploma in electrical engineering from Universidade do Estado de Santa Catarina (UDESC), Joinville, Brazil, in 2006. He has a M.Sc. degree in electrical engineering and a Ph.D. degree in automation and systems engineering, both obtained from Universidade Federal de Santa Catarina (UFSC), Florianópolis, Brazil, in 2008 and 2013, respectively. He is currently a researcher at the Dynamic Legged Systems (DLS) lab at Istituto Italiano di Tecnologia (IIT), Genoa, Italy. He is knowledgeable from the kinematic design to the control of hydraulic quadruped robots, with major expertise in dynamic motion generation and control. His research activities focus on proprioceptive-based and exteroceptive-based reactions, whole-body control, machine learning for locomotion, active impedance modulation, and loco-manipulation.



Domingo Esteban received the B.Sc. degree in industrial engineering from the Universidad Nacional de San Agustín, Arequipa, Peru, in 2009, the M.Sc. degree in robotics and automation from the Universidad Carlos III, Madrid, Spain, in 2014, and the Ph.D. degree in advanced and humanoid robotics from the Italian Institute of Technology (IIT), Genoa, Italy, in 2019. From 2019 to 2021, he was a Postdoctoral Researcher with the Dynamic Legged Systems Lab at IIT. He is currently working at ANYbotics A.G., Zurich, Switzerland. He is interested in machine learning for decision-making and motion control in robotics.



Octavio Villarreal received the M.Sc. degree in mechanical engineering track control engineering from TU Delft, The Netherlands, in 2016, and the Ph.D. degree from IIT and the University of Genoa, in 2019, working at the Dynamic Legged Systems (DLS) lab for his work on vision-based foothold adaptation and locomotion strategies for legged robots. He is currently a robotics research engineer at Dyson Technology Ltd.